applied optics

CCD detector performance of the space-borne Doppler wind lidar ALADIN during the Aeolus mission

Oliver Lux,[1,*] Robert Reichert,[1] Christian Lemmerz,[1] Nafiseh Masoumzadeh,[1,2] Denny Wernham,[3] Trismono Candra Krisna,[3] Denis Marchais,[4] Ray Bell,[5] Tommaso Parrinello,[6] and Oliver Reitebuch[1]

[1]Deutsches Zentrum für Luft- und Raumfahrt, Institut für Physik der Atmosphäre, 82234 Oberpfaffenhofen, Germany
[2]Current address: Max Planck Institute for Extraterrestrial Physics, 85748 Garching, Germany
[3]European Space Agency-ESTEC, Keplerlaan 1, 2201 AZ Noordwijk, The Netherlands
[4]Airbus Defence and Space (Toulouse), Rue de Cosmonautes, 31400 Toulouse, France
[5]Teledyne e2v, 106 Waterhouse Lane, Chelmsford Essex CM1 2QU, UK
[6]European Space Agency-ESRIN, Largo Galileo Galilei, 1, 00044 Frascati RM, Italy
*oliver.lux@dlr.de

Received 6 June 2024; revised 7 August 2024; accepted 12 August 2024; posted 13 August 2024; published 28 August 2024

The Aeolus mission, launched by the European Space Agency in August 2018, was a landmark in Earth observation by providing global wind profiles in near-real time using the first Doppler wind lidar in space: the Atmospheric Laser Doppler Instrument (ALADIN). Despite challenges such as systematic errors affecting data quality at the beginning of the mission, Aeolus surpassed its planned lifetime of three years and proved invaluable for weather prediction and scientific research until its conclusion in July 2023. A permanent challenge throughout the mission involved mitigating the impact of hot pixels on the ALADIN charge-coupled device (CCD) detectors on the wind data. The related dark current anomalies, which manifested as random telegraph signal noise and sporadic shifts in median dark current signal, necessitated the development of dedicated calibration techniques to minimize the induced systematic wind speed errors. The regular dark current calibrations of up to eight times per day yielded a comprehensive dataset that was used to categorize the hot pixels according to their characteristics and to derive statistical parameters that are of relevance for the reprocessing of the Aeolus data products. Following the end of the operational mission in April 2023, a series of specialized in-orbit tests, referred to as end-of-life (EOL) activities, provided valuable insights into the temperature dependence of the dark currents, shedding light on potential root causes of the hot pixels. Additionally, the EOL tests revealed other detector anomalies that had caused significant wind biases in certain altitudes following strong cosmic ray events in 2022. This work summarizes the performance of the ALADIN detectors during the Aeolus mission, with a focus on hot pixel characterization and mitigation strategies. Furthermore, it highlights findings from the EOL activities that are relevant for future space lidar missions and other satellite missions using CCD detectors.

https://doi.org/10.1364/AO.532217

1. INTRODUCTION

The Aeolus mission, led by the European Space Agency (ESA), made history as the first satellite mission dedicated to monitoring wind profiles of the global atmosphere. Launched on 22 August 2018, it successfully completed its mission on 30 April 2023, surpassing its planned three-year lifespan by 18 months. On 28 July 2023, the satellite was instructed with a last sequence of commands to ensure an assisted reentry into Earth's atmosphere. Equipped with the Atmospheric Laser Doppler Instrument (ALADIN), Aeolus pioneered European lidar technology and Doppler wind lidar into space [1–3]. ALADIN was a technical masterpiece which measured horizontal wind profiles in the line-of-sight (LOS) direction of the instrument globally from the surface of the Earth up to approximately 30 km [4]. Initially designed as a technology demonstration for future operational wind lidar missions, Aeolus quickly became an integral part of the global wind observing system, also thanks to the continuous improvement of the data product quality over the course of the mission [5–8]. Just two years after its launch, data from Aeolus were being used

in operational numerical weather prediction (NWP) models by key weather services, including the German Weather Service [9], Météo-France [10], and the European Centre for Medium-Range Weather Forecasts (ECMWF) [11]. The wind profile retrievals generated by the mission were shown to significantly enhance global NWP forecasts, akin to the impact of numerous other crucial operational satellite observing systems. This marked a significant milestone for a demonstrator mission, particularly noteworthy given that Aeolus contributed to less than 0.5% of the observations assimilated at ECMWF [12]. Furthermore, apart from numerous validation studies [13–19], Aeolus' global, height-resolved observations not only of winds but also of aerosol and cloud properties [20,21] have triggered investigations of atmospheric dynamics [9,22–24] and aerosol–cloud interactions [25–28]. As a result of the successful Aeolus mission, the ESA Ministerial Council Conference in November 2022 paved the way for an operational Aeolus follow-on mission, Aeolus-2, as a cooperation between ESA and EUMETSAT with launch in the 2030s.

As is typical for a lidar, ALADIN emitted pulses of laser light into the atmosphere where they interacted with molecules and particles. The backscattered light was collected with a telescope and guided to the receiver unit to derive the Doppler shift of the atmospheric return signal with respect to the frequency of the outgoing laser pulse using two spectrometers optimized for particulate and molecular backscatter spectra, respectively (details in the following section). These two ALADIN receiver channels incorporated sensitive accumulation charge-coupled device (ACCD) detectors for the analysis of the backscattered signals transmitted through the spectrometers on their two-dimensional imaging zones, which, after integration to a transfer row and accumulation of a settable number of pulses, allowed for a precise determination of the Doppler frequency shift. However, shortly after the mission started, single pixels of the detector's memory register used for the on-chip accumulation, so-called hot pixels (HPs), showed anomalous behavior with seemingly random jumps in the dark current signal that caused large errors in particular altitude bins of the wind and aerosol profiles [29]. Depending on the atmospheric backscatter signal intensity, dark current variations by a few tens of electrons induced wind bias variations by several meters per second. Consequently, a dedicated calibration mode had to be established to minimize the systematic error and ensure the high data quality of the Aeolus products [30]. The more time Aeolus spent in space, the more pixels of the ALADIN detector were affected, making it increasingly difficult to correct for the dark current fluctuations that occurred on different time scales for the individual HPs.

The origination of detector defects such as HPs is due to the harsh radiation conditions in space where high-energy particles such as cosmic electrons, heavy ions, neutrons, and protons are passing through CCDs [31] and other types of sensitive detectors. The exposure to these particles is most pronounced in the South Atlantic Anomaly (SAA) region, which extends from South America to southwestern Africa [32]. In this region, the Earth's magnetic field is weaker and more variable compared to other parts of the globe, resulting in higher levels of radiation interference with spacecraft electronics, especially in low Earth orbits below 1000 km altitude [33]. For instance, a considerable elevation in dark signal levels within the SAA region has been detected on the CCDs of the Hubble Space Telescope operating at an altitude of 550 km [34]. Effects on detectors beyond CCDs have also been documented, such as those observed on the photomultiplier tube aboard the CALIPSO satellite [35]. The generation of detector defects on backside-illuminated CMOS image sensors by irradiation with high-energy protons was investigated by Liu *et al.*, showing that radiation-induced HPs have a significant impact on pixel performance leading to dark signal non-uniformity and random telegraph signals [36].

Precise analysis of the detector performance is crucial to understand the limitations in the Aeolus data quality and to develop refined correction schemes to be applied in forthcoming reprocessing campaigns of the Aeolus products. Moreover, with regard to Aeolus-2 and ATLID on EarthCARE, both employing a similar detector technology, it is of great importance to assess the detector performance and limitations during the Aeolus mission to derive lessons learned for the preparation and implementation phases in the coming years. Therefore, this work focuses on the in-orbit performance of the Aeolus detectors, specifically addressing the various dark current anomalies encountered throughout the mission and their varying impacts on data quality. Beyond completing and refining the hot pixel classification reported by Weiler *et al*. [30], this paper offers new insights into the nature of the hot pixels based on special in-orbit tests conducted toward the end of the mission. Furthermore, it examines new anomalies on specific pixels that could not be adequately corrected by the aforementioned calibration mode.

In Section 2, the design and operating principle of the Aeolus detectors are outlined, followed by a description of the in-orbit procedures to assess the relevant detector properties (Section 3.A). The regular dark current characterization measurements formed the basis for a statistical analysis of the hot pixels, which is explained in Sections 3.B and 3.C. The results of the data analysis are presented in Section 4, providing an overview of all hot pixels and a classification with regard to their different temporal signatures. In Section 5, the temperature dependence of the dark current rates is discussed based on a dedicated instrument test, which was performed at the end of the mission. Another special operation gave insights into the anomalous behavior of two extraordinary hot pixels, which had particular impact on the Aeolus data quality (Section 6). Additional observations related to the Aeolus detector are summarized in Section 7. The paper closes with a concluding summary and outlook to upcoming space missions that will utilize similar detectors (Section 8).

2. ALADIN INSTRUMENT DESIGN

Aeolus orbited the Earth at an altitude of around 320 km and was equipped with a single instrument, the direct-detection wind lidar ALADIN. A powerful ultra-violet laser transmitter emitted ≈ 20-ns-short laser pulses with a vacuum wavelength of 354.8 nm at a pulse repetition rate of 50.5 Hz. During their path through the atmosphere, the laser pulses were backscattered from molecules and particles moving with the ambient wind, thereby causing a frequency shift due to the Doppler effect. The backscattered light was then collected by the same transmitting telescope and directed to the receiver unit, which

Table 1. Specifications and Important Parameters of the ALADIN ACCDs Measured On-Ground and In-Orbit

Specification	*Value*
Type	Thinned backside-illuminated accumulation Si-CCD
Area	Image zone: 0.43 mm × 0.43 mm − 16 × 16 pixels Memory zone: 0.43 mm × 0.75 mm − 32 × 25 pixels
Pixel size	Image zone: 27 µm × 27 µm Memory zone: 30 µm × 13.5 µm
Temporal resolution	2.1–16.8 µs/250–2000 m for atmospheric range gates (#1 to #24) 625 µs/1250 µs/3750 µs for solar background (range gate #25)
Parameter measured on-ground	*Value*
Quantum efficiency	0.85
Charge-transfer efficiency	0.999
Radiometric gain	Mie, 0.684 LSB/e^-; Rayleigh, 0.434 LSB/e^-
Parameter measured in-orbit	*Value*
Operating temperature	−30°C
Dark current signal rate (rms)	Mie, $(0.72 \pm 0.31)e^-s^{-1}$; Rayleigh, $(0.64 \pm 0.31)e^-s^{-1}$
Dark current signal noise (rms)	0.78 to 0.89 e^-
Readout noise (rms)	$(5.6 \pm 0.2)e^-$

consisted of two complementary channels. The Mie channel utilized a Fizeau interferometer to examine narrow-bandwidth return signals from clouds and aerosols, employing the fringe imaging technique [37]. For analyzing the broad-bandwidth atmospheric return from molecules, the Rayleigh channel comprised two sequential Fabry–Perot interferometers to derive the Doppler frequency shift by means of the double-edge technique [38,39]. Both channels used ACCDs, which enabled the accumulation of atmospheric backscatter signals from multiple successive laser pulses directly on the chip in a dedicated memory zone in order to reduce the impact of readout noise [30]. The ACCDs, manufactured as type CCD69 by Teledyne e2v and custom designed for the ALADIN instrument, exhibited a high quantum efficiency of 85% at 355 nm and low readout noise, which was not simultaneously achieved by available avalanche photodiodes or photomultipliers at the time of the instrument development. Some specifications of the ALADIN ACCDs including values describing the in-orbit performance are summarized in Table 1.

Figure 1 illustrates the ACCD design for the two Aeolus receiver channels. Each ACCD consisted of an illuminated image zone with 16 × 16 squared pixels (pixel size 27 µm × 27 µm) and a non-illuminated memory zone with 25 × 32 pixels (pixel size 30 µm × 13.5 µm). Sixteen of the 32 columns constituted the transfer section of the memory zone, while the other 16 columns interleaved between them formed the memory storage section in which the charge accumulation was performed (not shown in Fig. 1). The atmospheric signal, i.e., the Fizeau interferometer fringe and the two circular spots from the sequential Fabry–Perot interferometers, were recorded in the image zone of the Mie and Rayleigh ACCD, respectively.

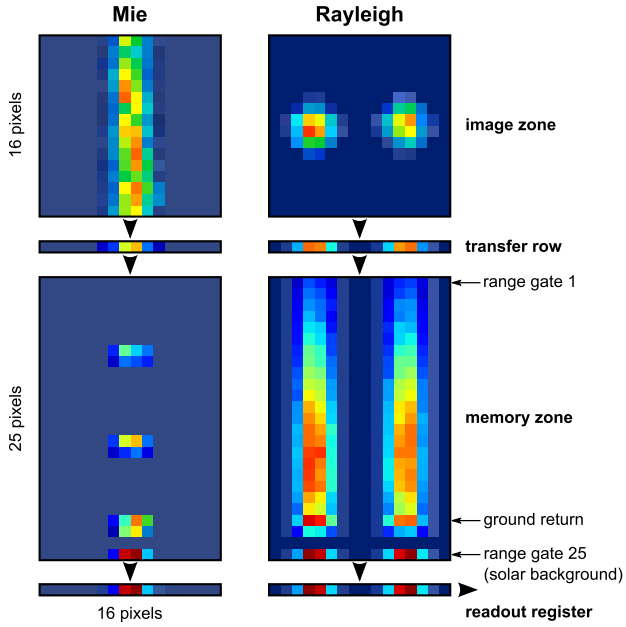

Fig. 1. Schematic of the Aeolus ACCD design with the image zone, transfer row, and memory zone for the Mie and Rayleigh channel (adapted from [40]).

The horizontal extent of the Rayleigh spots consistently covered five out of the eight columns in each hemisphere of the image zone, leaving the remaining three columns in both hemispheres unilluminated. In the Mie channel, the fringe from the narrowband return signal spanned approximately four to five columns, shifting back and forth across the image zone along the row direction depending on the frequency of the outgoing or backscattered signal. For most of the mission's duration, the frequency of the emitted laser pulse was adjusted to position the fringe in the center of the ACCD image zone under zero-wind conditions. Additionally, all Mie pixels were illuminated by the broadband molecular return signal and the solar background signal.

The atmospheric return signals were integrated over time according to the predefined vertical range gate setting with the vertical resolution of the range gates being determined by the integration time for each successive image. During the Aeolus operations, the range gate timings could be varied from 2.1 to 16.8 µs, which corresponded to a vertical sampling of 250–2000 m, respectively, considering the 35° off-nadir viewing angle of the instrument. The charges generated in the image zone were subsequently moved downward row by row at a 16 MHz line advance frequency, where they were binned in the transfer row before being transferred into the transfer section of the memory zone. The process of binning and capturing into the memory zone, which took about 1.0 µs, was repeated for the charges from the next range gate until the 25 rows of the memory zone of the ACCD were filled; i.e., the signals from the 25 vertical range gates were captured in the transfer section of the memory zone. It is worth noting that the signal from the subsequent range gate already illuminated the image zone during the transfer process of the previous one, which resulted in an overlap of adjacent range gates and a vertical smearing of the signal correspondingly.

The charges from the transfer columns were horizontally shifted to the corresponding pixels in the interleaved storage columns of the memory zone. Following each accumulation sequence over the required number of laser shots, the charges that had been accumulated into the memory storage zone were read out via the readout register at a very low frequency of 48 kHz to minimize readout noise. Before accumulating the next series of laser shots, the image zone, memory transfer section, and memory storage section were flushed at 1 MHz by pulsing all clocks 50 times, pushing all stray charges into the serial register's lateral dump drain. The accumulated signal was converted into a voltage at the ACCD output and transferred to the detection electronics unit (DEU), where it was amplified and digitized with 16-bit accuracy while an electronic offset voltage was applied to prevent negative values during digitization. This so-called detection chain offset (DCO) was generated by a special clocking sequence during the readout process and was quantified by two prescan and two postscan pixels in each row of the ACCD. The signals read out in these four virtual pixels only contained the few charges generated in the register itself during readout and could hence be used for the DCO correction of the signals measured in the 16 active pixels of each row of the image or memory zone. The amplified signals including the DCO were finally converted into units of least significant bits (LSB). The conversion rate of this process, known as radiometric gain or system gain, was $g_{\mathrm{Mie}} = 0.684\ \mathrm{LSB/e^-}$ and $g_{\mathrm{Ray}} = 0.434\ \mathrm{LSB/e^-}$ for the Mie and Rayleigh channels, respectively. Further details on the design and operating principle of the Aeolus ACCDs were provided by Weiler *et al*. [30], while a comprehensive overview of CCDs was published by Janesick [41].

The on-chip signal accumulation over a certain number of laser pulses (P) resulted in the so-called measurement scale. During ground processing, a defined number of measurements (N) was then combined to so-called observations with a length of 12 s. During a large part of the Aeolus mission, P was set to 19 and N was set to 30. In December 2021 and April 2022, the P/N settings were first changed from 19/30 to 38/15 and then from 38/15 to 114/5, respectively, in order to increase the signal levels on measurement scale relative to the readout noise.

In contrast to the first 24 (atmospheric) range gates, the integration time for row #25 of the memory zone was considerably longer for the purpose of measuring the solar background signal in order to correct the atmospheric signals for the solar background contribution. While the default integration time was set to 3750 µs, it was shortened to 1250 µs and finally to 625 µs in April 2022 to avoid saturation of the pixels in row #25, which occurred as a result of the change in the P/N settings mentioned above. For the analysis presented in the following, row and column indices are used to describe the pixel position on the ACCDs. For example, Mie [15,13] refers to row #15 and column #13 (counting starts at one) of the memory zone of the Mie ACCD.

3. METHODS

A. Dark Current in Memory Zone Characterization

Already during the commissioning phase of the Aeolus mission in 2018, it turned out that dark current signal anomalies on single hot pixels of the two ACCDs detrimentally impacted the quality of the wind and aerosol data products, leading to wind errors of up to several meters per second. Hot pixels are generally described as pixels with a permanent increase of the dark current. This increase is mostly caused by radiation-induced effects that can be categorized into three groups: ionization damage, displacement damage, and transient effects.

Ionization damage involves an increase of trapped charges in the dielectric materials of the CCD and thus an increased dark current as well as a shift in the optimum operating voltages of the CCD. However, this effect is largely avoided by efficient shielding of the optical sensors from ionization radiation.

Displacement damage is caused by higher-energetic particles, mainly protons, that can pass through the shielding and the detectors. This may displace atoms from their lattice and create vacancy-interstitial pairs, some of which form stable displacement damages in the lattice, thereby increasing the dark current. In addition, displacement damage may also introduce random telegraph signal (RTS) noise, which is characterized by sudden step-like transitions between two or more discrete dark current levels at random and unpredictable times.

Transient effects occur due to ionization-induced generation of charges within the detectors and do not cause permanent damage. Nevertheless, since transient effects might be visible as spurious signal spikes on one or more pixels, the affected measurements must also be rejected by the quality control of the lidar signal analysis. Apart from radiation-induced effects, so-called clock-induced charges (CICs) can cause an increase of the dark signal. Here, a spurious signal is generated by transferring measurement signals through the CCD and contributes to the dark signal. When clocking the charges through a register, there is a small probability that additional charges are created, which eventually manifest as additional dark signals.

Initially, characterization of the dark current on the memory zone (DCMZ) was only foreseen at the beginning of the mission before the laser was switched on. However, as the number of hot pixels steadily increased during the first months after the launch of Aeolus, a dedicated dark current calibration mode was introduced and carried out throughout the mission on a regular basis in order to mitigate the systematic errors. To this end, the so-called DUDE (down under dark experiment) was established as a new procedure to characterize the DCMZ during continuous laser operation. During DUDE measurements, which were regularly performed starting from 26 November 2018, the range gate timing settings are adjusted such that the return signal would be acquired from below the Earth's surface. In this manner, dark current signals of all pixels of the memory zone could be measured without lidar signal contributions and negligible solar background signals provided that the DUDE was conducted at geolocations with a sun elevation angle below −4°. The geolocation was thus updated based on the seasonal sun position. The frequency of the DUDEs was increased over the course of the mission to two per day from 17 December 2018 onwards, to four per day from 22 January 2019 onwards, to seven per day from 6 September 2021, and finally to eight per day from 30 October 2021 onwards to keep up with the increasing number of HPs.

At the end of the nearly five-year mission lifetime of Aeolus, the total number of hot pixels amounted to 75, from which

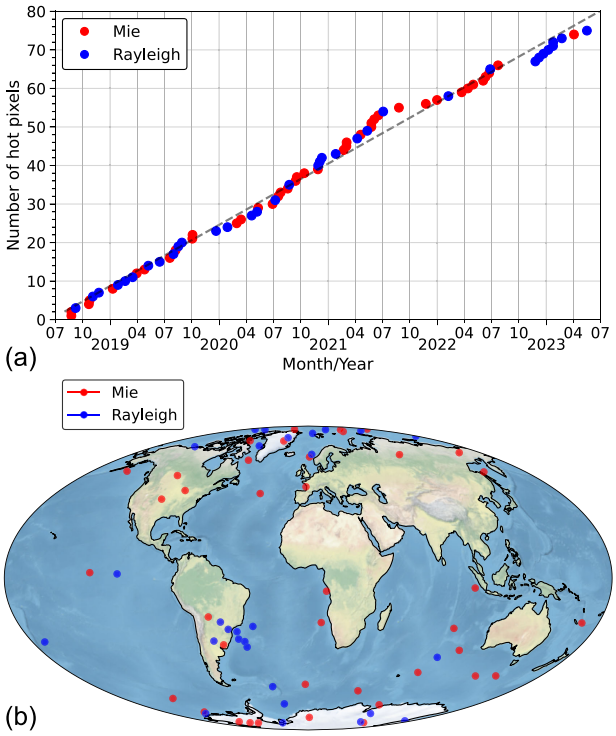

Fig. 2. (a) Temporal evolution of the number of hot pixels over the mission timeline. Mie hot pixels [16,15] and [24,03] were already present before launch. (b) Geolocation of the satellite during the first activation of the individual hot pixels (only if data of the exact activation time is available). Mie and Rayleigh hot pixels are indicated as red and blue dots, respectively. The map is shown in Mollweide projection to ensure area equality.

41 were activated on the Mie channel and 34 on the Rayleigh channel ACCD, respectively. This corresponds to about 10% of all pixels of the two memory storage zones ($2 \times 16 \times 24 = 768$) when considering the 24 atmospheric range gates only. Their activation, i.e., the moment from which on the dark current rate was permanently above the noise level, followed a nearly linear trend with a time difference between successive hot pixel onsets of (23 ± 21) days. Figure 2(a) shows that larger departures from linearity were present during the mission, e.g., in summer/autumn 2021 or between July and November 2022 when there was no new hot pixel for 124 days. However, no correlation was found between the hot pixel onset rate and space weather activity, nor with any platform or instrument parameters. In particular, the hot pixel activation could not be correlated with the K index, which is a measure of the disturbances of the horizontal component of the Earth's magnetic field; i.e., no threshold of activity could be identified [30]. It is also noticeable that, after the long gap in 2022, seven Rayleigh pixels became hot before another Mie hot pixel emerged.

The geolocation of the satellite during the onset of the individual hot pixels is depicted in Fig. 2(b), indicating a preponderance around the poles and the SAA region. The latter is characterized by a reduced intensity of the Earth's magnetic field at altitudes between 200 and 800 km, resulting in a stronger exposure of the Aeolus satellite (about 320 km altitude) to cosmic radiation. It was also found that transient events are accumulated around the SAA region, occurring about three times more frequently in the box between 40° to 60°S latitude and 60° to 30°W longitude compared to the rest of the globe. Nevertheless, the relative frequency of such events is very low with only 0.24% of all measurements being affected, equally distributed among all pixels on both detectors. Further studies revealed that in about half of the events, more than one pixel showed a spurious intensity peak at the same time. In some cases, even more than 10 pixels were simultaneously affected, resulting in stripes on the memory zone that display the propagation of the grazing particle across the detector. It is worth mentioning that the two detectors were shielded in a cuboid shape with average alumninum equivalent shielding thicknesses of 9.2 mm and 4.5 mm for the Rayleigh and Mie ACCD, respectively. The larger shielding thickness for the Rayleigh ACCD may explain the lower number of hot pixels compared to the Mie channel detector.

B. Step Detection

The DCMZ data from about 8500 DUDE measurements were used to analyze the dark current levels on the 24×16 pixels in each of the memory zones of the Mie and Rayleigh ACCD, i.e., excluding the solar background range gate #25, and their evolution during the mission period. For this purpose, the measured signal was corrected for the detection chain offset (DCO) and the solar background. The fact that the number of detector signal accumulations per observation (P/N settings) was changed several times during the mission lifetime was considered when summing up the dark current levels. Quality checks were performed to ensure negligible influence of solar background and to filter out measurements when the detection range was accidentally not completely below the Earth's surface leading to contamination of the upper range gates (=memory zone rows) with atmospheric return signal.

The identification of sudden changes in the dark current time series of individual pixels, e.g., related to transitions between multiple RTS levels, can be regarded as the task of partitioning the time series into a number of segments. This task is usually tackled by an offline change point detection approach [42] where a given multivariate time series is retrospectively analyzed to identify the moments in time when main characteristics of the time series have changed. The segmentation of the DCO- and solar background-corrected DCMZ time series is performed by using the ruptures Python package [30,42,43]. Identifying sudden shifts in the dark current signal involves selecting the optimal segmentation of the signal based on a cost function that must be minimized. This function includes an additive linear term that increases with the number of detected segments, controlled by the smoothing parameter or penalty term β. Consequently, the number of detected segments is sensitive to the β value, with more segments detected at lower β values and fewer segments at higher β values. Weiler *et al*. used a β value of 23.0 LSB, thoroughly tuned and selected based on visual inspection of the entire dataset [30]. However, this penalty term resulted in an unexpectedly small number of dark current transitions, with segment lengths biased towards longer lifetimes.

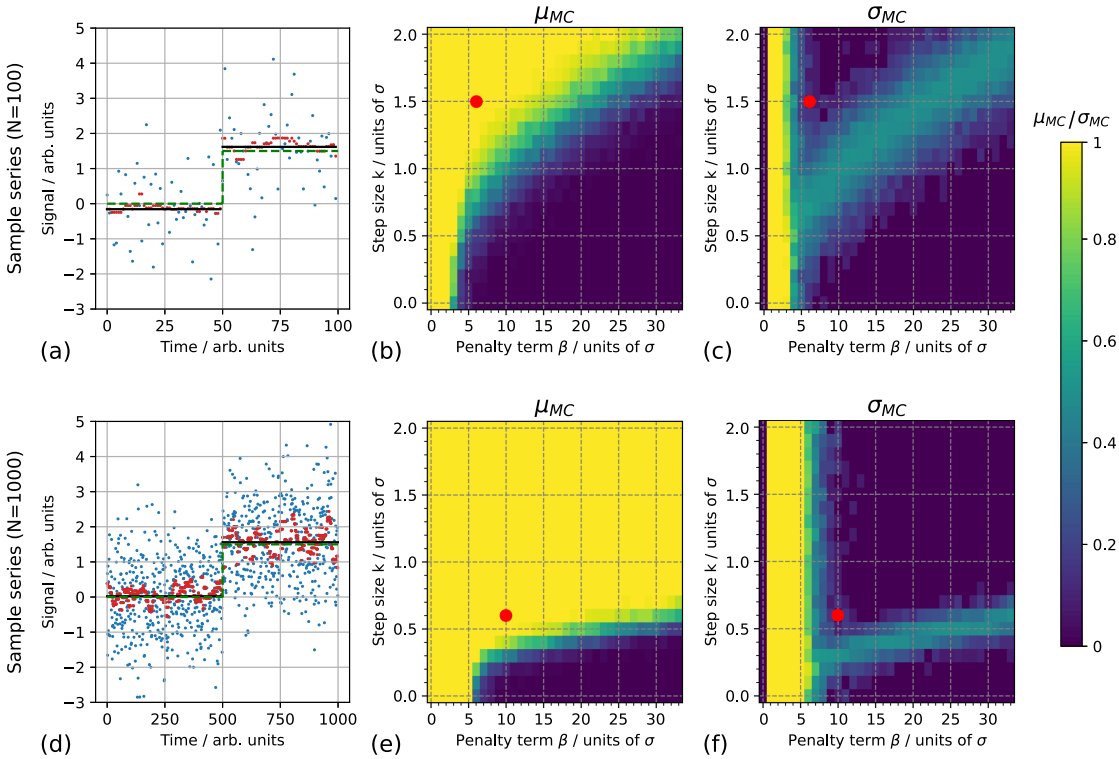

Fig. 3. Example for the segmentation sensitivity study using a Monte Carlo simulation with 200 repetitions: sample series with step size $k = 1.5\sigma$, $\beta = 10\sigma$ and Gaussian noise $\sigma = 1$ for (a) $N = 100$ and (d) $N = 1000$. Blue dots mark original data, red dots show 20-units median filtered data, green dashed line marks the mean input, and black lines represent the detected segments. The middle and right panels depict (b), (e) average number of detected steps μ_{MC} and (c), (f) standard deviation σ_{MC} as a function of penalty and step size for $N = 100$ (top) and $N = 1000$ (bottom). The optimum values for β and k for the respective sample sizes are indicated by red dots.

C. Sensitivity Study

In order to find an appropriate penalty term β in the segmentation process, we present a series of Monte Carlo (MC) simulations. Multiple simulations were carried out not only to investigate the robustness of the β value, but also to derive a relationship between the detectable step size and the statistical lifetime of RTS levels.

We first model a sample series as

$$s_i = \begin{cases} 0 + r_i, & \text{for} \quad 0 < i < \frac{N}{2}, \\ k\sigma + r_i, & \text{for} \quad \frac{N}{2} < i < N, \end{cases} \tag{1}$$

where σ is the standard deviation of a normal distribution, which is taken to be 1 in our MC simulations, r_i are random numbers originating from a normal distribution of mean $\mu = 0$ and standard deviation σ, and $k\sigma$ is the step size. The sample series consists of N data points where a regular temporal spacing δt relates to the lifetime as $\tau = \frac{N}{2}\delta t$. An example for a sample series of length $N = 100$ and a step size of 1.5σ is shown in Fig. 3(a). In the next step, the *ruptures* algorithm is applied changing the penalty term β from 0σ to 33σ in steps of 1σ. Figure 3(a) illustrates the identified segments and segment-wise 20-units median filtered data. The process of generating a sample series and subsequent segmentation with variable penalty term is repeated 200 times.

As a result, Figs. 3(b) and 3(c) show the number of detected steps averaged over the 200 MC simulations and the corresponding standard deviation as a function of β and k. For large $\frac{\beta}{k}$ ratios the step is not identified, i.e., $\mu_{\mathrm{MC}} = 0$. With a decreasing $\frac{\beta}{k}$ ratio the correct number of steps is identified, i.e., $\mu_{\mathrm{MC}} = 1$, but the standard deviation is relatively large ($\sigma_{\mathrm{MC}} \approx 0.5$). The most appropriate penalty term is found when the standard deviation is as small as possible and the number of detected steps is close to 1, since s is modeled with one step. Therefore, we identify the minimum of $\sigma_{\mathrm{MC}} + |\mu_{\mathrm{MC}} - 1|$. In addition, we ask for a minimum that is associated with the smallest step size possible. The optimal β value for $N = 100$ is found at $\beta = 6\sigma$ and corresponds to a detectable step size of about 1.5σ. For a MC simulation with $N = 1000$ we find an optimal β value at $\beta = 10\sigma$ with a corresponding detectable step size of 0.6σ [see Figs. 3(d)–3(f)]. For comparison, [30] have set $\beta \approx 33\sigma$. Therefore, we must assume that depending on the lifetime and step size the number of identified segments as presented in [30] is underestimated. The resolvable step size and the average lifetime for each hot pixel are provided in Tables 2 and 3 for the Mie and Rayleigh ACCD, respectively.

4. OVERVIEW OF HOT PIXELS AND CLASSIFICATION

Based on the dark current analysis and the segmentation approach described in the previous section, the individual hot pixels were classified, and several parameters that are relevant for the Aeolus data quality were derived. The outcome of the

Table 2. Selected Parameters of the Hot Pixels on the Mie ACCD[a]

Hot Pixel	Activation Date, UTC Time (if available)	Classification	Most Likely Step/LSB	Lifetime/Hours
[01,02]	03/03/2021, 02:01:40	Mean shifts	–	944
[02,03]	11/06/2022, 14:25:46	RTS	56	13
[02,10]	28/02/2020, 20:35:40	RTS	167	38
[02,15]	24/10/2018, 07:00:43	RTS	41	80
[03,03]	10/05/2020, 13:31:28	RTS	75	19
[03,04]	21/02/2021, 00:35:52	Mean shifts	–	837
[03,15]	12/10/2020, 06:17:16	Mean shifts	–	925
[04,01]	02/03/2021, 06:30:04	Mean shifts	–	1355
[04,03]	03/10/2019, 22:21:52	Mean shifts	–	2097
[04,11]	19/07/2019, 20:07:04	RTS	13	28
[05,11]	03/10/2019, 05:16:16	Mean shifts, later RTS	51	108
[05,13]	09/01/2019, 14:22:55	RTS	11	51
[06,03]	03/06/2021, 13:07:49	RTS	126	75
[07,02]	17/07/2020, 03:22:16	RTS	247	33
[08,06]	25/08/2021, 06:38:37	RTS	48	14
[08,07]	17/08/2020, 19:04:52	Mean shifts, later RTS	98	62
[08,13]	17/09/2020, 06:20:52	Mean shifts	–	2240
[09,13]	08/08/2019, 05:04:28	RTS	26	15
[09,14]	24/05/2021, 22:40:49	RTS	67	64
[10,13]	26/04/2019, 00:27:22	RTS	23	72
[12,13]	30/12/2021, 20:28:58	Mean shifts	–	895
[13,05]	26/11/2020, 21:10:04	RTS	69	89
[13,07]	28/06/2020, 00:33:16	Mean shifts	–	155
[13,09]	21/10/2018, 17:19:07	Mean shifts and RTS	47	21
[14,02]	23/03/2022, 12:06:22	RTS	56	25
[14,14]	23/06/2022, 15:53:34	Mean shifts	–	277
[15,06]	14/03/2020, 09:02:40	RTS	14	87
[15,08]	03/04/2023, 15:58:50	Mean shifts	–	37
[15,12]	19/04/2021, 04:00:13	RTS	51	11
[16,05]	23/11/2021, 09:11:58	RTS	47	17
[16,15]	Pre-launch	Mean shifts, later RTS	11	108
[17,05]	17/06/2021, 05:05:25	RTS	45	14
[17,07]	13/04/2022, 11:29:22	RTS	12	24
[18,02]	13/09/2020, 04:36:52	RTS	12	19
[18,04]	03/06/2022, 12:22:46	RTS	62	34
[19,01]	23/07/2022, 07:49:46	RTS	17	13
[19,15]	01/05/2022, 08:25:22	RTS	49	34
[20,02]	31/03/2019, 03:39:34	Mean shifts and RTS	65	72
[24,02]	25/05/2021, 23:40:01	RTS	17	43
[24,03]	Pre-launch	Mean shifts	–	13
[24,13]	24/07/2020, 23:31:16	Mean shifts	–	864

[a]The classification is also visualized in Fig. 7. The statistical parameters were derived from the segmentation approach.

analysis is exemplarily shown in Fig. 4 for Mie pixel [06,03], which became hot on 3 June 2021 with an activation level of 149 LSB. Before its activation, the median dark current level was around 10 LSB (black line) with a standard deviation of $\sigma_{\mathrm{obs}} = 25$ LSB on observation level (blue dots). Considering the number of measurements $N = 30$ per observation in this phase of the mission, the dark current fluctuations account for $\sigma_{\mathrm{meas}} = 22\ \mathrm{LSB}/\sqrt{30} \approx 4.0$ LSB on measurement level. When also taking into account the noise of the DCO ($\sigma_{\mathrm{DCO}} \approx 1.5$ LSB), which is subtracted from the raw signal levels, the readout noise can be estimated: $(\sigma^2_{\mathrm{meas}} - \sigma^2_{\mathrm{DCO}})^{1/2} \approx 3.7$ LSB, which corresponds to $5.4e^-$ (Table 1). The noise of the dark current as well as of the DCO and solar background causes negative dark current values for individual observations after DCO and solar background subtraction, as seen in the time series in Fig. 4.

About one month after its onset, Mie pixel [06,03] showed a two-level RTS behavior, as indicated by two distinct peaks in the distribution of dark currents at 43 LSB and 169 LSB [Fig. 4(b)]. As the dark current almost only fluctuated between these two levels, there is a pronounced peak at 126 LSB in the transition energy (or jump size) distribution [Fig. 4(c)]. The noise that is introduced by the RTS transitions is characterized as a Poisson process such that the probability for a transition as function of time t and average lifetime τ is given as $p(t) = \frac{1}{\tau} \exp(-\frac{t}{\tau})$. We fit this sigmoid function to the distribution of lifetimes in order to derive the average lifetime τ.

Table 3. Selected Parameters of the Hot Pixels on the Rayleigh ACCD[a]

Hot Pixel	Activation Date, UTC Time (if Available)	Classification	Most Likely Step/LSB	Lifetime/Hours
[01,07]	20/02/2019, 07:57:22	RTS	19	76
[03,02]	08/05/2019, 21:01:22	Mean shifts, slow drift, RTS	20	17
[03,13]	22/08/2020, 21:04:28	RTS	64	47
[03,14]	07/04/2021, 15:47:25	mean shifts, later RTS	68	17
[05,02]	04/11/2018	mean shifts	–	1560
[05,10]	25/01/2021, 12:32:16	RTS	25	16
[05,13]	23/01/2023, 13:19:31	RTS	33	22
[06,01]	22/02/2023	Mean shifts and RTS	–	87
[07,15]	18/04/2020, 22:26:28	RTS	5	39
[08,10]	28/01/2020, 21:55:28	Mean shifts	–	1822
[09,12]	06/02/2022, 21:20:34	RTS	11	24
[10,16]	07/12/2022, 16:55:19	RTS	18	16
[11,02]	07/09/2018	RTS	16	66
[11,08]	15/06/2019, 18:40:34	RTS	19	73
[11,16]	17/03/2019, 06:50:34	RTS	32	10
[13,03]	03/07/2021, 15:41:25	RTS	33	41
[13,06]	23/01/2023, 23:32:19	RTS	19	14
[13,15]	26/06/2022, 21:49:22	RTS and strongly reduced charge storage ratio	13	9
[14,02]	07/05/2020	mean shifts and RTS	25	75
[14,05]	25/11/2022, 06:13:31	RTS	38	5
[15,04]	24/11/2018	Mean shifts	–	662
[15,16]	07/01/2023, 21:05:07	RTS	14	25
[16,04]	22/12/2022, 09:33:19	RTS and strongly reduced charge storage ratio	5	70
[17,10]	03/12/2020, 04:35:04	Mean shifts	–	934
[18,08]	11/05/2021, 05:01:37	RTS	27	12
[20,02]	01/08/2019, 03:54:16	RTS	31	16
[20,10]	27/01/2019	Mean shifts	–	187
[20,16]	17/08/2019, 08:37:04	Mean shifts	–	972
[22,10]	27/11/2020, 20:53:28	RTS	9	18
[23,06]	10/12/2020	RTS	9	24
[24,04]	29/08/2019, 08:13:16	RTS	33	55
[24,06]	21/12/2019, 17:06:04	RTS	114	48
[24,10]	06/07/2020, 21:41:16	RTS	10	59
[24,11]	17/05/2023	RTS	2	36

[a]The classification is also visualized in Fig. 7. The statistical parameters were derived from the segmentation.

The average lifetime of the RTS levels for Mie pixel [06,03] is 3.1 days (75 h). The treatment of two-level RTS hot pixels such as Mie [06,03] during the data reprocessing is comparatively easy, as the jump size is foreseeable, which facilitates the differentiation of RTS noise from other noise sources, e.g., due to atmospheric signal variations. Other hot pixels that show two-level RTS behavior are, for the Mie ACCD, [02,10], [02,15], [05,11], [07,02], [08,07], [09,13], [09,14], [13,05], and [20,02] and, for the Rayleigh ACCD, [14,02], [24,04], and [24,06].

A different characteristic was observed for Mie hot pixel [03,15] (see Fig. 5). Its activation occurred on 12 October 2020 with a jump of the dark current by 64 LSB. In contrast to the example above, there were only sporadic shifts of the mean dark current level but no RTS signatures. The frequency of these shifts even decreased over the mission. This behavior was also evident for most of the other hot pixels of this class, namely, for the Mie ACCD, [01,02], [03,04], [04,01], [04,03], [08,13], [12,13], [13,07], [14,14], [15,08], [24,03], and [24,13] and, for the Rayleigh ACCD, [05,02], [08,10], [15,04], [17,10], [20,10], and [20,16]. Thanks to their low activity, these hot pixels have a rather small detrimental impact on the Aeolus data products.

Some hot pixels show a combination of RTS jumps and shifts of the mean dark current. One extreme example is Mie pixel [13,09], which shows a superposition of multi-level RTS with sporadic mean shifts. This pixel became hot on 2 November 2018 with an activation value of 320 LSB. The peak finding algorithm reveals 7 RTS levels [Fig. 6(b)]. The distribution of transition differences shows two major peaks at 47 LSB and close to 200 LSB [Fig. 6(c)]. It appears that interaction between RTS levels takes place in three-level clusters. In 2020, there was a lower level cluster of three RTS levels at 194 LSB, 251 LSB, and 312 LSB and an upper level cluster of RTS levels at 448 LSB, 481 LSB, and 526 LSB. Intra-cluster transitions result in the peak at transition differences of 47 LSB, while the second

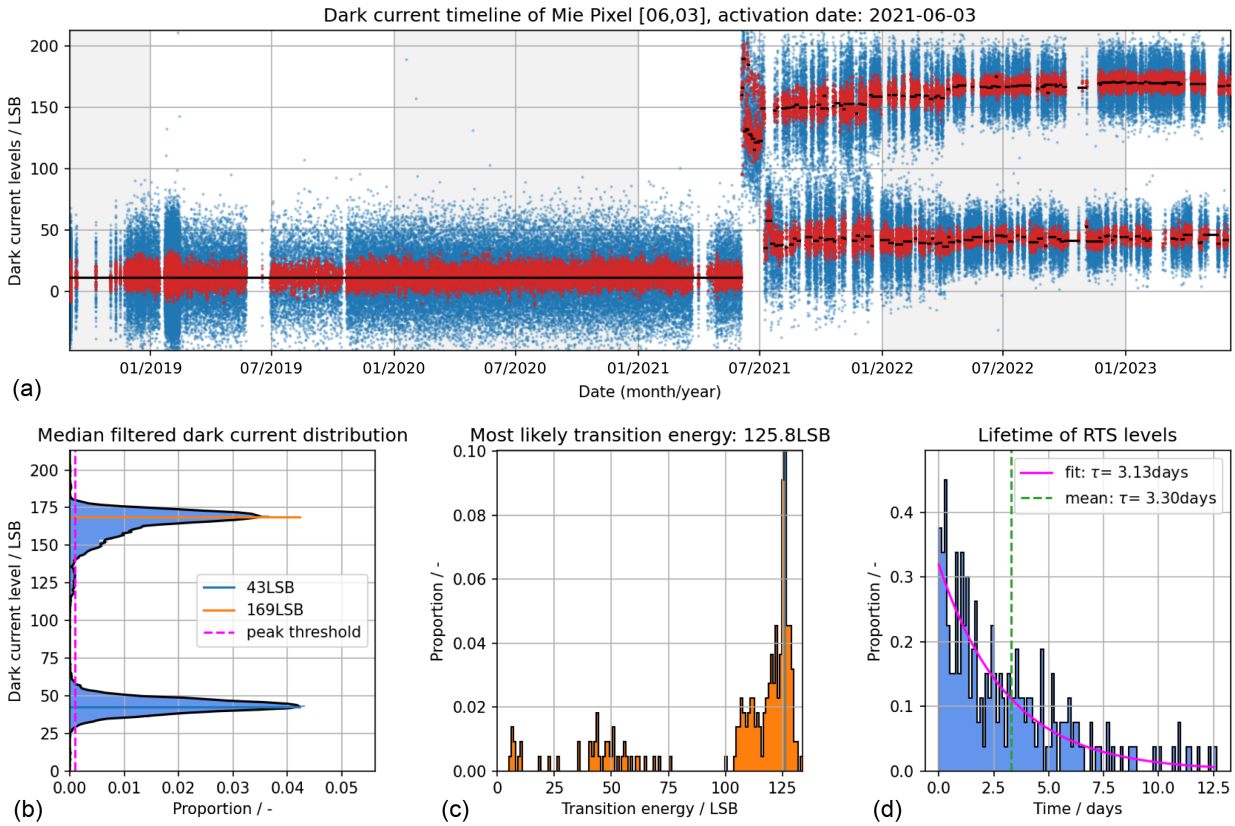

Fig. 4. Characterization of Mie hot pixel [06,03]: (a) time series of the dark current on observation level after subtraction of offsets (DCO, solar background). The blue dots represent the original resolution, while the red dots are obtained after applying a median filter over 20 observations. The black dots indicate the identified segments. (b) Distribution of the median filtered data after activation of the HP. The peaks indicated by the horizontal line were retrieved by a Gaussian kernel density estimation (KDE) in combination with a peak finding algorithm (threshold marked by the magenta dashed line). (c) Distribution of transition energies (or step sizes). The step sizes corresponding to the identified RTS levels in panel (b) are additionally drawn as vertical blue lines. The magenta dashed line marks the sensitivity limit. (d) Distribution of segment lengths (or RTS lifetimes). The magenta curve represents a sigmoid function fit. The corresponding average lifetime is given in the legend. The dashed green vertical line marks the arithmetic average lifetime, which is more meaningful for hot pixels that show less than 100 transitions (here: 219 transitions).

peak close to 200 LSB is related to inter-cluster transitions. After 2020, two superimposed sporadic mean shifts in March 2021 and October 2021 led to an even more complicated RTS level system.

Apart from the three categories of hot pixels shown above (mean shifts, RTS, combination of both), there are also some special cases that exhibit additional characteristics. For instance, Rayleigh hot pixel [03,02], activated on 8 May 2019, showed RTS behavior and two mean shifts in the dark current level in February and October 2022. In addition, the dark current levels were slowly drifting to lower values between July 2020 and the first mean shift in February. Consequently, the distribution of dark current levels is strongly broadened.

The two Rayleigh hot pixels [13,15] and [16,04] stand out from all the others, as they introduced large wind biases in the corresponding range gates despite the correction for the DCMZ applied during the wind retrieval based on the DUDE measurements. The reason was traced back to a charge storage anomaly, which will be discussed in Section 6.

Lists with all Mie and Rayleigh hot pixels are given in Tables 2 and 3, respectively. Besides the introduced classification and activation date and time, the lists provide the most likely step size between RTS levels and the average lifetime of the dark current levels.

The classification of the hot pixels is also visible in Fig. 7, which additionally illustrates their location on the memory zones of the Mie and Rayleigh ACCDs as well as the order of their onset. The maps reveal that the hot pixels are not randomly distributed but show a certain clustering both locally and temporally. For instance, Mie hot pixels [17,05], [16,05], [17,07], and [18,04] are very close together and were activated within one year between June 2021 and June 2022. Conversely, there are no Mie hot pixels in the ACCD rows #21 through #23. The same holds for rows #2, #4, #12, #19, and #21 of the Rayleigh ACCD, whereas there were even four hot pixels in row #24. Overall, 3/4 of the HPs show RTS behavior (Mie, 29 out of 41; Rayleigh, 28 out of 34).

5. TEMPERATURE DEPENDENCE

Following the end of nominal operations of ALADIN on 30 April 2023, a series of special tests, referred to as end-of-life (EOL) activities, was performed until July 2023 to address a number of instrument-related and scientific questions. As one of

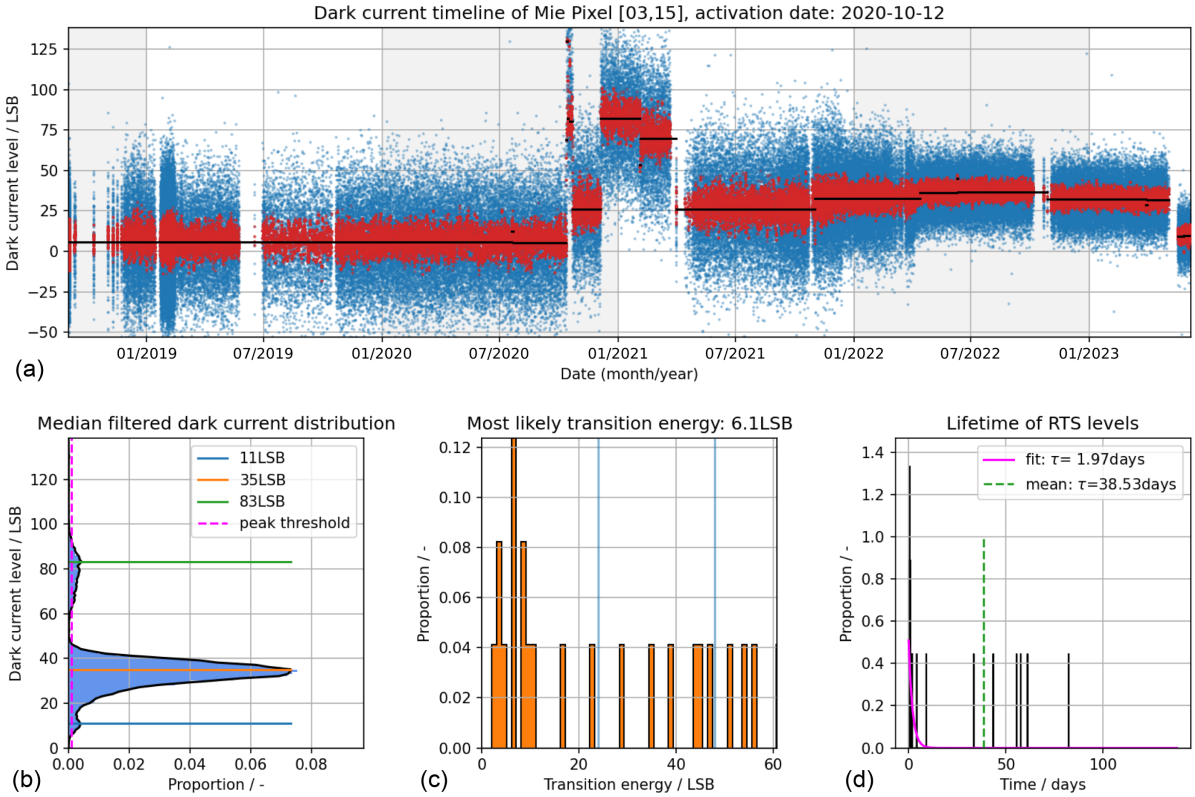

Fig. 5. Characterization of Mie hot pixel [03,15]. Description of the panels, see Fig. 4.

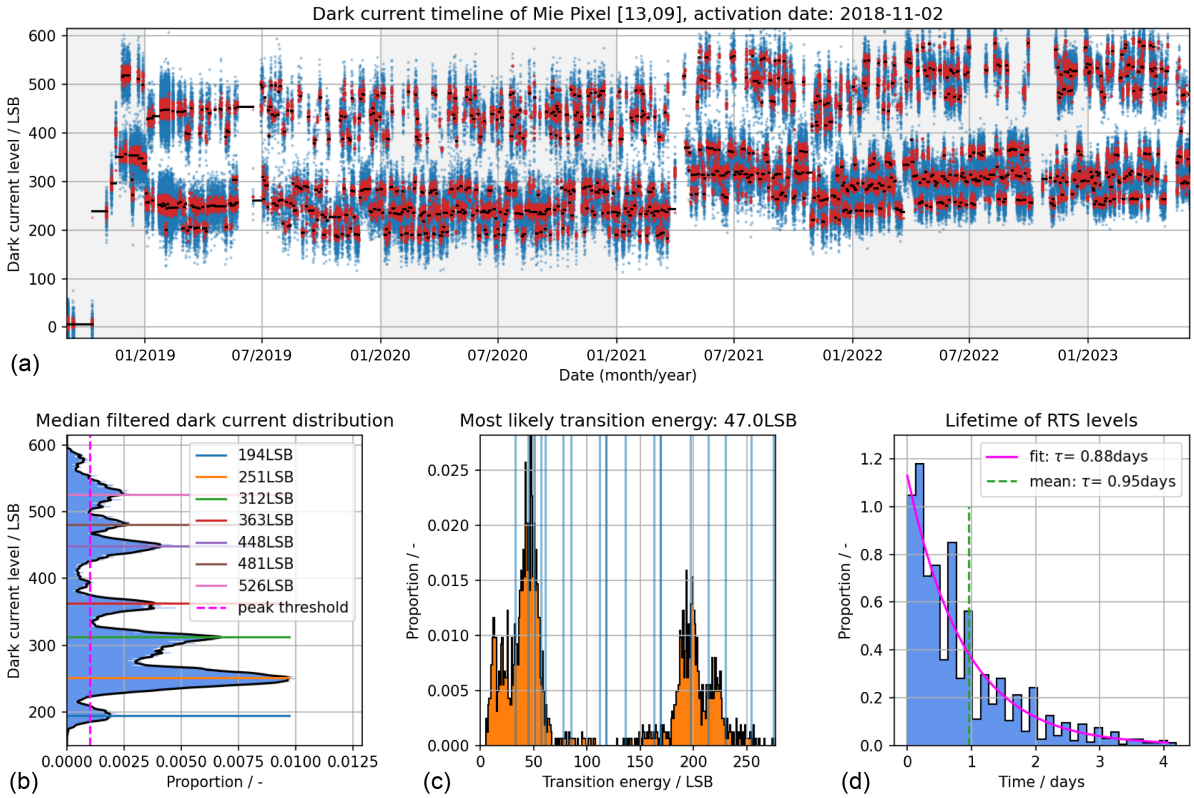

Fig. 6. Characterization of Mie hot pixel [13,09]. Description of the panels, see Fig. 4.

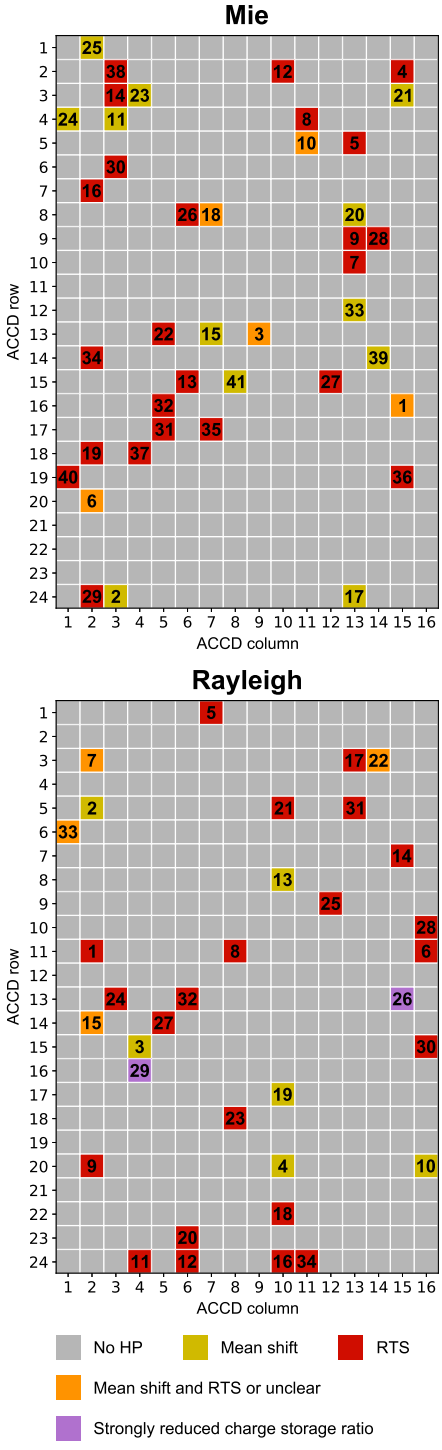

Fig. 7. Map of hot pixels on the Mie ACCD (top) and the Rayleigh ACCD (bottom). The color coding refers to the classification of the individual hot pixel characteristics (see text), while the number indicates the order of the activation on the respective detector.

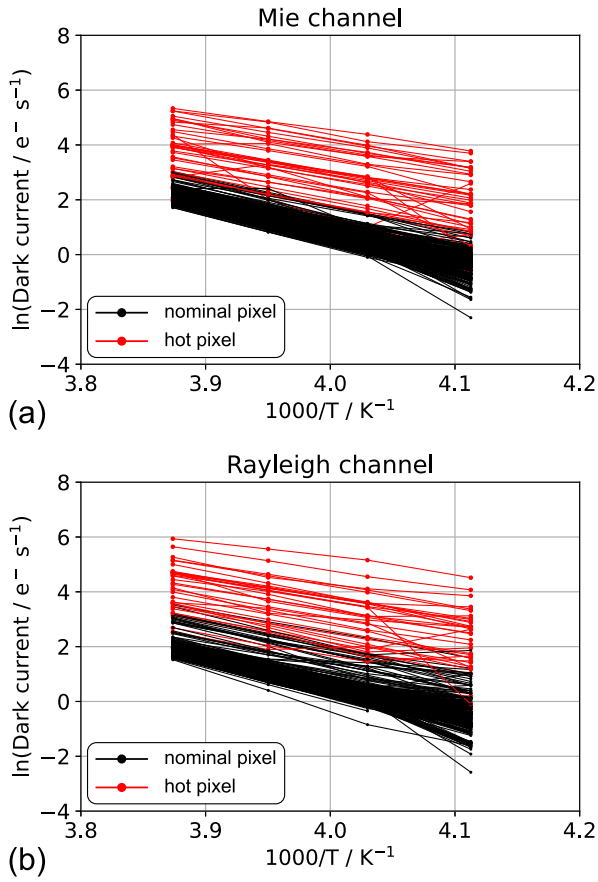

Fig. 8. Arrhenius plots (natural logarithm of dark current rates versus inverse absolute temperature) for all pixels of (a) Mie and (b) Rayleigh ACCD. Hot pixels are indicated in red.

the EOL tests, the temperature dependence of the dark currents in the memory zone of the Rayleigh and Mie ACCDs was investigated with particular focus on those pixels that became hot during the mission. For this purpose, the ACCD temperature was increased from the nominal value of −30°C to −15°C in steps of 5 °C. The non-nominal temperature settings at −25°C, −20°C, and −15°C were kept for 4.5 h (about three orbits), each which enabled a precise determination of the dark current levels on all pixels of the memory zone. However, the periods were too short to investigate the influence of temperature on the RTS time constants on the hot pixels, let alone the probability of their activation.

Note that, in 2020, a similar test was performed with the airborne prototype of the Aeolus payload, the ALADIN Airborne Demonstrator (A2D) [5,44–46], which employs the same types of ACCDs in its Mie and Rayleigh receiver as the satellite instrument. Analysis of the A2D ACCDs revealed one pixel (Mie [15,10]) with slightly increased dark current levels (<3e⁻), which is sometimes referred to as a "lukewarm" pixel. In contrast to ALADIN, the A2D detector temperature was varied in the range from −35°C to −15°C, i.e., at even lower temperature than used operationally (also −30°C like ALADIN). Reducing the ALADIN ACCD temperature to −35°C was considered too risky because of the limitation of the thermal system managing the ACCDs by means of a thermoelectric cooler.

Based on the test data from the EOL activity that was carried out on 15–16 May 2023, the median dark current rate was calculated for all individual pixels at the four temperature settings, and the temperature dependence was studied for the nominal and hot pixels. The temperature dependence was found to follow the Arrhenius law, as expected from [47]

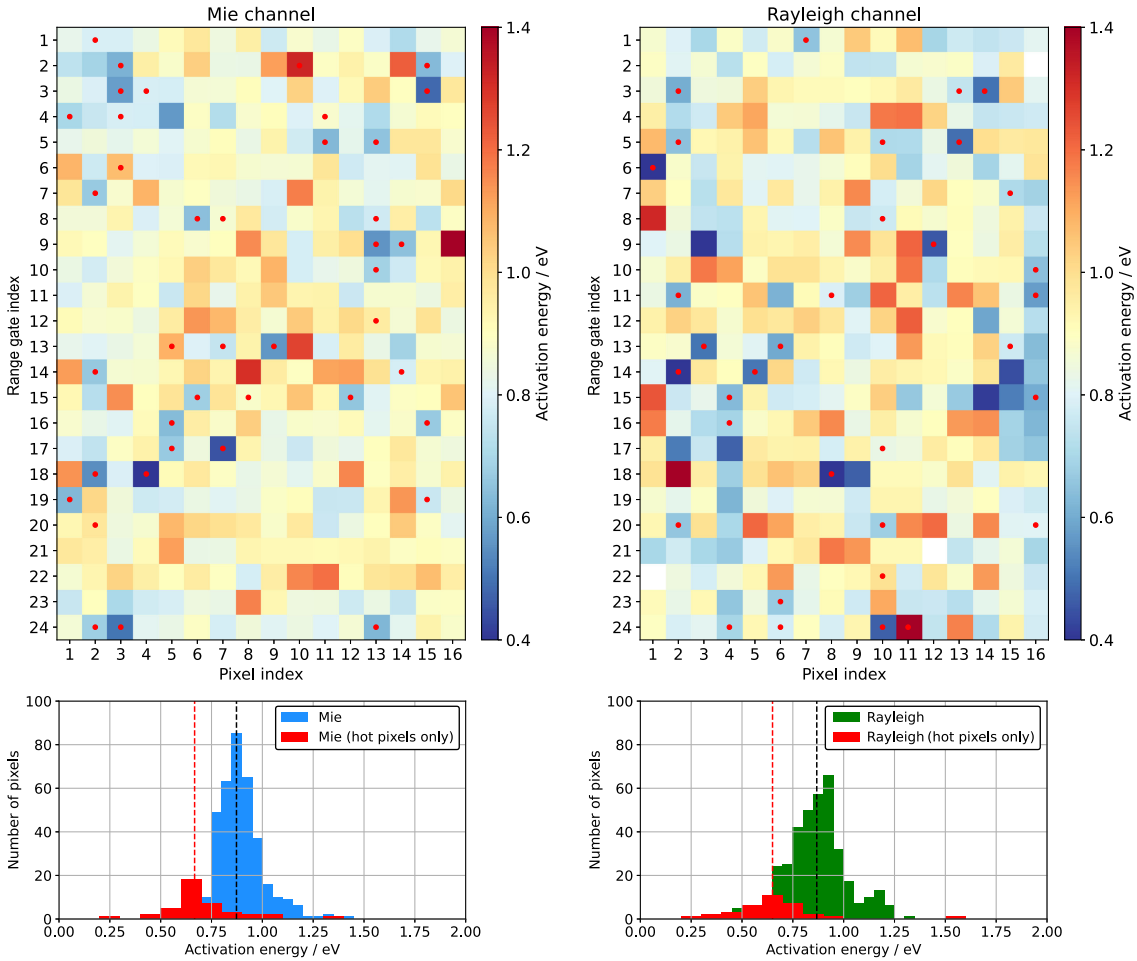

Fig. 9. Activation energy of the pixels from the memory zone of the Mie (left) and Rayleigh ACCD (right). Hot pixels are indicated by a red dot. The corresponding histograms are shown in the bottom panels.

$$\mathrm{DC} = \mathrm{DC}_0 \exp\left(E_a / k_\mathrm{B} T\right), \tag{2}$$

with DC being the dark current rate in $\mathrm{e^-s^{-1}}$ and E_a being the activation energy, while k_B denotes the Boltzmann constant. The activation energy can be determined from a linear fit when plotting the natural logarithm of the dark current rate against the inverse temperature in a so-called Arrhenius plot, as depicted in Fig. 8 for all pixels from the Mie and Rayleigh ACCD. This procedure yielded maps of the activation energies that are shown in Fig. 9 together with the corresponding histograms for the two ACCDs. Note that a few HPs underwent RTS transitions during the temperature test that manifest as departures from linearity for some of the red lines in Fig. 8. Due to the limited dataset available from the special EOL activity, the distorted results of the linear fits for those HPs were still considered in Fig. 9 but did not affect the median values.

The values are relatively consistent across both ACCDs with median values of $E_{a,\mathrm{Mie}} = (0.87 \pm 0.09)$ eV and $E_{a,\mathrm{Mie}} = (0.87 \pm 0.13)$ eV, respectively. The energies are systematically smaller by about 25% for the hot pixels: $E_{a,\mathrm{Mie,hot}} = (0.67 \pm 0.13)$ eV and $E_{a,\mathrm{Ray,hot}} = (0.65 \pm 0.16)$ eV. This result is expected for surface dark currents that are caused by radiation-induced displacement damages, which strongly supports the assumption that the dark current anomalies are "conventional" hot pixels and not caused by CICs. More specifically, the activation energies align closely with those of a phosphorus-vacancy (PV) dipole, measuring 0.70 eV, i.e., 0.44 eV lower than the silicon conduction band (refer to chapter 8 in [41]). The occurrence of PV defects was also found in several studies on proton-irradiated CCD sensors [48–50].

It is interesting to note that the activation energies were also determined for the A2D, yielding similar values: $E_{a,\mathrm{Mie,A2D}} = (1.00 \pm 0.03)$ eV and $E_{a,\mathrm{Ray,A2D}} = (1.03 \pm 0.03)$ eV. However, these energies could only be derived for the range gate that measures the solar background signal due to the different data processing for the A2D where the DCO is detected in one particular range gate instead of the 4 virtual pixels on the edges of the ACCD image zone, resulting in slightly negative DCO-corrected signal levels on the atmospheric range gates in the absence of atmospheric backscatter.

When excluding the hot pixels, the dark current rates at the nominal ACCD temperature of −30°C were $\mathrm{DC_{Mie,-30}} = (0.72 \pm 0.31)\mathrm{e^-s^{-1}}$ and $\mathrm{DC_{Ray,-30}} = (0.64 \pm 0.31)\mathrm{e^-s^{-1}}$ (Fig. 10), i.e., similar for both detectors when considering the spread among all pixels. Note that the radiometric gain factors of $g_\mathrm{Mie} = 0.684\,\mathrm{LSB/e^-}$ and $g_\mathrm{Ray} = 0.434\,\mathrm{LSB/e^-}$ were used for conversion from LSB to $\mathrm{e^-}$ (see also Table 1). In addition,

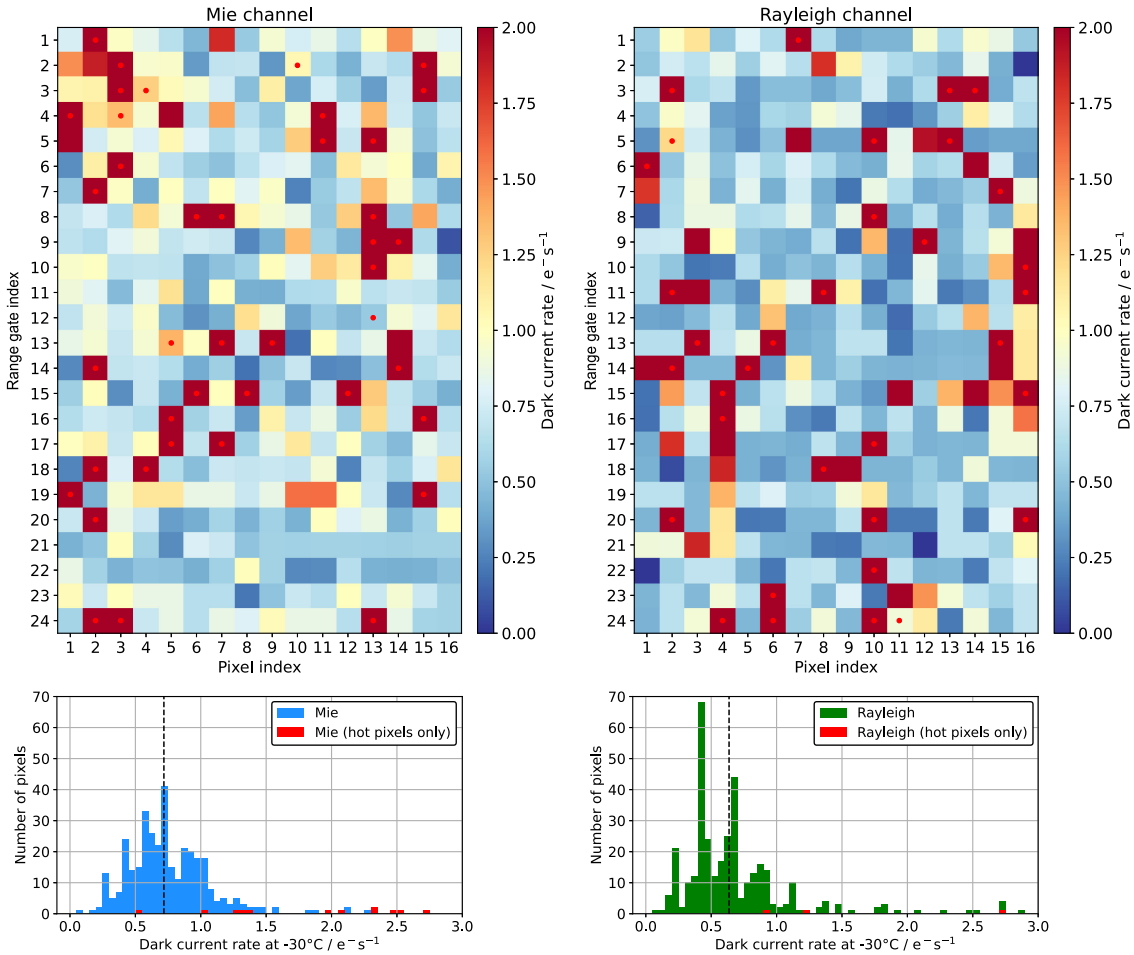

Fig. 10. Dark current rates at −30°C of the pixels from the memory zone of the Mie (left) and Rayleigh ACCD (right), as determined from the Arrhenius law. Hot pixels are indicated by a red dot. The corresponding histograms are shown in the bottom panels. Note that most hot pixels have dark current rates greater than $3e^{-}s^{-1}$ and are thus not shown in the histograms.

the number of pulses P = 114 and the pulse repetition frequency (50.5 Hz) need to be considered in the calculation of the dark current rates.

The derived temperature dependence allowed for the extrapolation of the dark current rates to −50°C, which is the operational temperature expected for the Aeolus-2 detectors, yielding $DC_{Mie,-50} = (0.017 \pm 0.012)e^{-}s^{-1}$ and $DC_{Ray,-50} = (0.015 \pm 0.012)e^{-}s^{-1}$. This corresponds to a reduction by a factor of ≈ 40 compared to −30°C for the nominal pixels. Due to the smaller activation energies, i.e., temperature sensitivities, of the hot pixels, their dark current rates are only reduced by a factor of ≈ 17. Nevertheless, 47 of the 75 hot pixels at −50°C (63%) would have dark current rates $<0.8\ e^{-}s^{-1}$ and are thus comparable to the dark current rates of normal pixels at −30°C during the Aeolus mission. However, they would still stand out with increased dark currents compared to that of normal pixels at −50°C. Aside from the reduced dark current rates, the RTS time constants are assumed to be larger at a lower temperature, which could, however, not be extrapolated based on the EOL dataset due to the short test period.

6. CHARGE STORAGE NON-UNIFORMITY

The implementation of the regular DCMZ measurements, i.e., DUDEs, in early 2019 largely eliminated the systematic errors that were introduced by the dark current fluctuations on the steadily increasing number of hot pixels. Remaining biases in the near-real time wind data were only present in periods between an RTS transition and the following dark current calibration that was then used for the processing of the next orbits. In reprocessing campaigns the wind data quality could be further improved by retrospectively applying DCMZ corrections to orbits between the RTS transitions and the next DUDE measurement [51]. In early 2023, however, a large persistent Rayleigh wind bias of more than 7 ms^{-1} was noticed in range gate #16. This was traced back to hot pixel [16,04], which became hot on 22 December 2022. In contrast to the other HPs, its onset involved a signal saturation not only on the pixel itself, but also on the three pixels below in the same ACCD column, suggesting a particularly strong exposure to cosmic radiation. Following this event, pixel [16,04] exhibited a reduced amount of charges stored in this memory zone pixel compared to other pixels of the same column #4 but other rows (=range gates) after normalization to the respective integration time. Consequently,

the underestimation of the signal levels led to a systematic error of the Rayleigh signal in range gate #16, and thus to a wind bias, which could only be partly compensated for by switching off the DCMZ correction for this pixel, thereby increasing the signal levels by the amount of the dark current offset. Subsequent investigations of this anomaly revealed that Rayleigh hot pixel [13,15], which had become hot already on 26 June 2022, also showed this charge storage anomaly and thus increased bias, albeit to a lesser extent (≈ 1 ms^{-1}), which is why it was only discovered afterwards. Like pixel [16,04], this pixel went into saturation upon its activation, which points to a damage causing the observed effect.

For further investigation of the anomalous behavior of the two special HPs, an extended DCMZ measurement was carried out over multiple orbits in the frame of the EOL activities on 15 May 2023 when the instrument was in so-called laser burst warm up (LBWU) mode without emitting laser pulses. During the 6-h-long test four different solar background integration times (0.625, 1.25, 2.5, and 3.75 ms) were applied while adapting the P/N settings to avoid saturation of the background pixels at high solar background conditions around the North Pole. The test data were used to compare the measured signal levels on individual memory zone pixels of the 24 atmospheric range gates in relation to those in the background range gate #25. In the following, these parameters will be referred to as charge storage ratio (CSR). Apart from the different dark current on each pixel, especially on the HPs, the signal levels, produced solely from solar background radiation in the Northern Hemisphere part of each orbit, should be equal across the ACCD columns after normalization to the integration time of the respective range gate. Therefore, it is expected that the slope from a linear fit that is applied to a correlation plot of signal levels among pixels of the same column is very close to 1.0. This is the case for nominal pixels such as Rayleigh pixel [12,15], as depicted in Fig. 11(a), showing the correlation of its signal levels against those measured on the corresponding pixel of the background range gate (pixel [25,15]), normalized to the integration time of range gate #12. While the slope from the linear fit, which can be identified with the CSR, is 1.0 for all P/N settings and background integration times for the nominal pixel [12,15], it is considerably reduced for the two special hot pixels mentioned above and highlighted in purple in Fig. 7.

For pixel [16,04], the measured signals are about 15% lower at P = 114 and even 38% lower at P = 19 than those measured on the corresponding pixel [25,04] of the background range gate [Fig. 11(b)]. The effect is less pronounced on pixel [13,15], where CSR is reduced by 4% at P = 114 and by 25% at P = 19 [Fig. 11(c)]. The scatterplots also show that the CSR not only depends on the P/N settings, but also varies with the signal levels; i.e., the relationship is not purely linear, which complicates a potential correction for this effect. Moreover, since it is visible on measurement level, it already occurs during the on-chip signal accumulation. The fact that the CSR is lower for a smaller number of accumulations P is counter-intuitive, as one would expect that deficiencies in the accumulation of charges get more pronounced as P increases. Discussions with ACCD manufacturer, Teledyne e2v, led to the hypothesis that recombination of charges may be a possible root cause. However, this has not been verified, yet.

Apart from the two exceptional Rayleigh hot pixels where the charge storage anomaly was most pronounced, the EOL dataset also allowed for the determination of the CSR of all illuminated pixels on the Rayleigh ACCD, i.e., those on columns #2 through #6 and columns #11 through #15. Following the same approach of the pixel-wise analysis of the signal levels in the atmospheric range gates in relation to the background range gate, the CSR was derived from a linear fit for the setting that was used at the end of the operational phase of the Aeolus mission (background integration time: 0.625 ms, P = 114, N = 5). The resulting CSR map is shown in the right panel of Fig. 12 together with the maps obtained from the beginning of the mission on 2 September 2018. Since the calculation of the CSR requires sufficient signal intensity on the pixels and the absence of atmospheric backscatter signals, i.e., only strong solar background, such maps could only be derived on a few occasions during the mission when the instrument was in LBWU mode. The maps and corresponding histograms illustrate the non-uniformity of the CSR across the Rayleigh ACCD of about ±2%, which has an impact on the

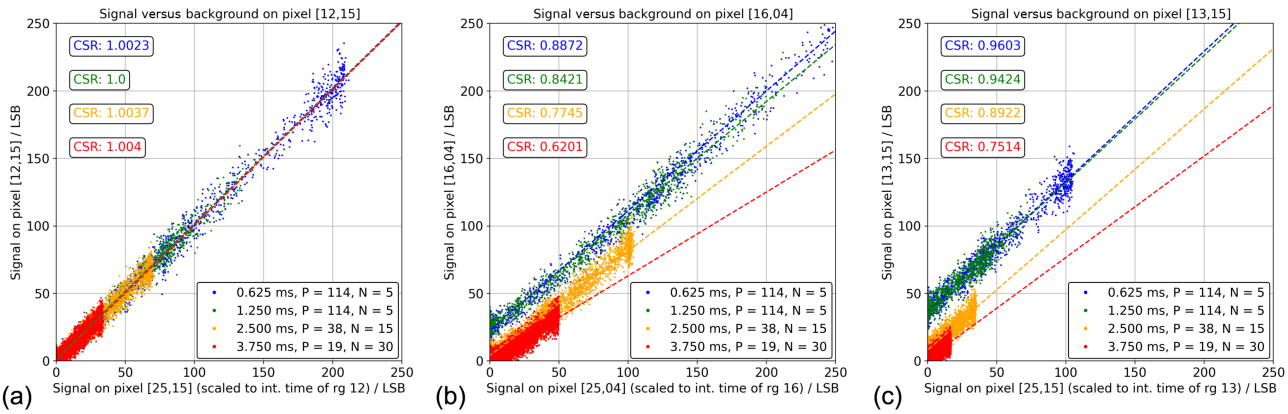

Fig. 11. Scatterplots correlating the signal levels measured on individual pixels in the atmospheric range gates of the Rayleigh ACCD memory zone against those from the same column in the background range gate #25. The data are subdivided into four different settings of the background integration time and P/N values, as indicated by the colors and plot legend. Linear fits are shown as dashed lines with the slope representing the charge storage ratio of the studied pixel. The analysis is exemplary shown for (a) nominal pixel [12,15] and the two special hot pixels (b) [16,04] and (c) [13,15].

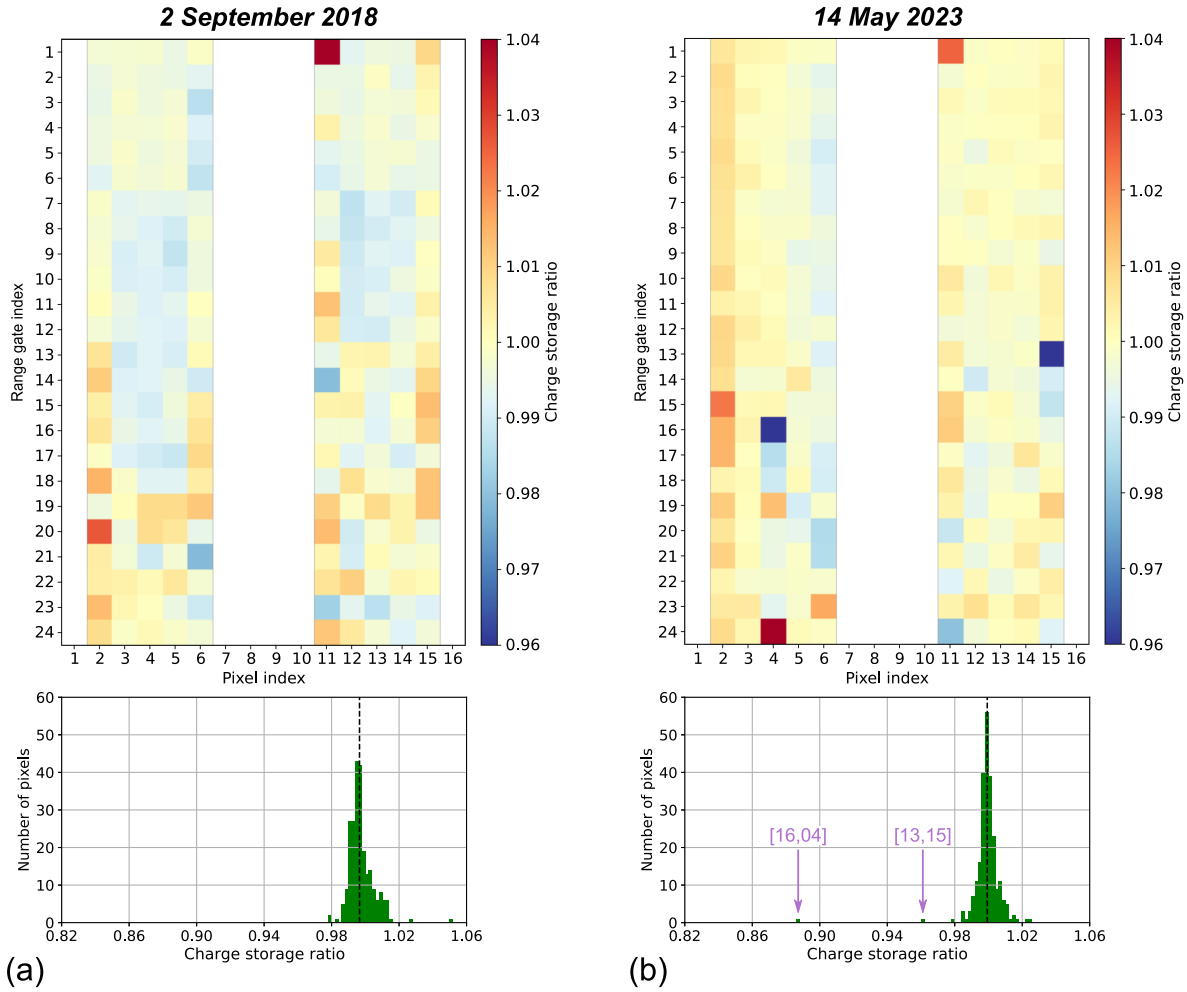

Fig. 12. Charge storage ratio (CSR) map for the Rayleigh ACCD obtained (a) at the beginning of the mission on 2 September 2018 and (b) at the end of the mission on 14 May 2023. Determination of the CSR requires sufficient signal intensity on the respective pixels. Therefore, data are only available on illuminated pixels, i.e., in columns #2 through #6 and columns #11 through #15. The distribution of the CSR across the ACCD memory zones is shown in the histograms below.

Rayleigh signal and ultimately on the Rayleigh wind error in the respective range gates. Extreme cases are the aforementioned pixels [13,15] and [16,04] that appeared in 2022.

The derived CSR map from 2023 was used in combination with Aeolus Level-1A (L1A) data from one day (30 April 2023) to calculate the change in the Rayleigh wind bias when correcting for the non-uniformity. To this end, the L1A DCO-corrected Rayleigh signal levels were scaled pixel-wise by dividing the CSR value per pixel, before applying the correction for solar background and dark current, in analogy to the Level-1B processor. Afterwards, the Rayleigh signals and Rayleigh responses were derived for each range gate. Then, the difference in Rayleigh response with and without the application of the CSR map was determined and finally converted to horizontal line-of-sight (HLOS) wind speed by using parameters from Rayleigh response calibrations. As a result, the wind speed difference caused by the CSR non-uniformity was obtained per range gate. This procedure is illustrated in Fig. 13, which depicts the Rayleigh signal levels per pixel in column #16, averaged over all observations from 30 April 2023. The two maxima in the two hemispheres of the ACCD correspond to the transmission peaks of the two Fabry–Perot interferometers, referred to as filters A and B, that constitute the Rayleigh channel spectrometer (Fig. 1). Due to the degraded CSR of pixel [16,04] being located in the center of filter A, the absolute change in the signal level when dividing by the CSR map is particularly large, thereby increasing the total signal in the left hemisphere I_A by 5.6% with the correction. Consequently, the Rayleigh channel response R, which is defined as the signal contrast between the two filters, $R = (I_A - I_B)/(I_A + I_B)$, is considerably shifted. The response shift translates into a wind speed difference of almost 12 ms^{-1}.

Apart from the large impact on range gate #16 introduced by pixel [16,04], the analysis revealed range-gate-dependent wind speed variations of about ± 2 ms^{-1}, especially in the lower range gates where the CSR of the pixels in the corresponding rows shows larger variability compared to the upper part of the ACCD, as seen in Fig. 12. In particular, a vertical smearing of the CSR is visible along column #4 starting from the anomalous hot pixel [16,04], which was activated by the cosmic ray event

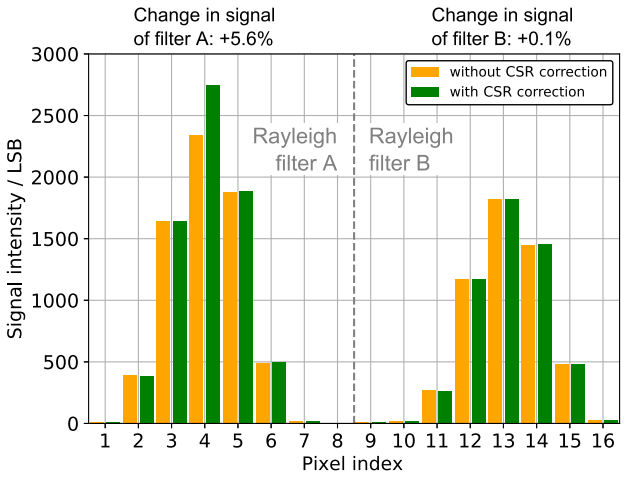

Fig. 13. Rayleigh signal in range gate #16, averaged over all observations from 30 April 2023, without (orange) and with consideration of the CSR map (green) in the processing. The CSR correction has the largest impact on pixel #4 due to the anomalous pixel [16,04], which increases the signal in the left hemisphere (filter A) by 5.6%, thereby strongly affecting the Rayleigh channel response.

on 22 December 2022 mentioned above, strongly affecting not only this pixel, but also the ones below to a smaller extent.

Interestingly, the wind speed dependence per range gate shows qualitative agreement with the Rayleigh-clear [11,52] wind bias profile that was derived from Aeolus Level-2B (L2B) data, although the latter exhibited smaller error variations than what was simulated based on the derived CSR map. Figure 14(a) displays the L2B Rayleigh-clear wind error with respect to the ECMWF model background per orbit and per range gate for the week between 12 and 19 April 2023. Starting from 18 April 2023, the wind retrieval was performed with a new processor baseline (B16) which, amongst other changes, included the option to disable the DCMZ correction for selected ACCD pixels. In the Aeolus mission, a processor baseline refers to a specific tagged version of the retrieval algorithms and operational processors used to handle and analyze the satellite's data, encompassing all steps from initial calibration and correction to final product generation. Over the mission's course, 16 different baselines have been used, with two more (B17 and B18) planned for phase F after the end of the mission to reprocess flight data and further enhance the quality and consistency of the data products over the complete mission timeline.

At the time of the baseline change from B15 to B16 and the corresponding implementation of the processor update, the underlying reason for the large wind bias in range gate #16 was not yet understood. Simulation of the Rayleigh response change introduced by not subtracting the enhanced dark current for pixel [16,04], similar to the calculations described above, yielded a reduction of the systematic error. Therefore, it was decided to switch off the DCMZ correction for this anomalous pixel in B16. As seen from Fig. 14(a) and the corresponding bias profiles for B15 and B16 in Fig. 14(b), this action significantly decreased the bias in range gate #16 from about 7 to 1.5 ms^{-1}. However, it is important to note that the omission of the DCMZ correction did not resolve the root cause of the bias, but only partially counteracted the low CSR of pixel [16,04] by retaining the enhanced dark current level which is ≈ 30 LSB on measurement level at P = 114 [see y-axis intercept in Fig. 11(b)]. This explains the remaining wind bias in range gate #16 and suggests that the systematic error varies over the orbit depending on the atmospheric backscatter and solar background signal measured

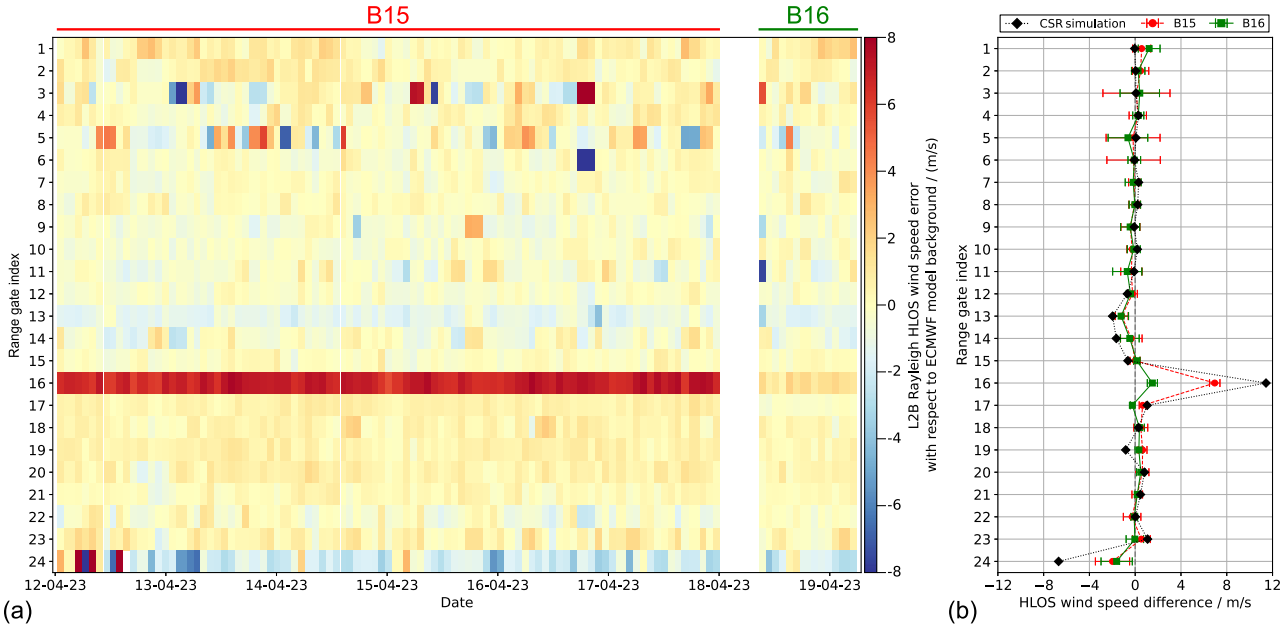

Fig. 14. (a) Aeolus L2B Rayleigh-clear wind error with respect to the ECMWF model background per range gate for the period between 12 and 19 April 2023. On 18 April 2023, the new baseline B16 came into effect including, amongst other processor changes, a switch-off of the DCMZ correction for the Rayleigh pixels [16,04] and [17,04]. (b) Profiles of the Rayleigh wind error per range gate before (red) and after the baseline change (green) from B15 to B16. The data points are the median values over all orbits plotted in (a), while the error bars represent the standard deviation. The black curve shows the calculated wind speed difference with and without application of the CSR map into the processing of the raw signal level, as described in the text.

on pixel [16,04] with the latter not being adequately corrected for due to the low CSR.

The wind bias profiles in Fig. 14(b) also illustrate the effect of Rayleigh pixel [13,15], which causes a negative bias of about 1.2 ms^{-1} in range gate #13. The different sign compared to range gate #16 is due to the pixel being located on the right hemisphere of the Rayleigh ACCD (filter B of the Rayleigh spectrometer), hence causing an opposite response shift than pixel [16,04]. As pixel [13,15] is located on the right edge of Rayleigh spot B, the contribution to the total signal intensity of the right hemisphere I_B is comparatively small, which alleviates the influence of the reduced CSR on the Rayleigh response. It is also notable that Rayleigh pixel [24,04] has a particularly high CSR value [see Fig. 12(b)], which is likely the reason for the negative wind bias of almost 2 ms^{-1} in range gate #24. These results suggest that the CSR non-uniformity is relevant for the Aeolus data quality and requires further investigation, which is foreseen for phase F of the Aeolus mission from 2024 through 2028. As a lesson learned for Aeolus-2, extended dark measurements over multiple orbits, as done on 14 May 2023, should be performed on a regular basis to characterize the CSR of the detectors and to potentially correct for their non-uniformity. Also, the temporal stability of this effect needs to be studied during mission development to determine the required frequency of such in-orbit calibrations. Since only illuminated pixels can be monitored using the procedure explained above, a dedicated ground characterization of all pixels is recommended before integration.

It should be noted that a comparable analysis of the CSR for the Mie channel ACCD was hindered by the too weak solar background signal levels after being transmitted through the Fizeau interferometer, which is optimized for narrowband signals. Nevertheless, a potential CSR non-uniformity of the Mie ACCD may also slightly effect the determination of the Mie fringe centroid position and hence the Mie wind speed. Since the Mie channel response is less sensitive to signal variations than the Rayleigh response, the impact is expected to be much smaller. However, the derivation of cloud and aerosol optical properties, such as backscatter and extinction coefficients, which are retrieved from the Mie channel signal levels and are included in the Aeolus Level-2A product [53], may be affected.

Besides the impact of the CSR non-uniformity on the wind results, Fig. 14 illustrates the temporal variability of the wind bias in certain range gates. Increased bias fluctuations are visible in range gates #3 and #5, where the standard deviation over the 80 orbits before the switch from B15 to B16, represented by the red horizontal error bars, accounts for 2.9 ms^{-1} and 2.4 ms^{-1}, respectively. The standard deviation for the other atmospheric range gates is below 1 ms^{-1}, except for range gate #24 (1.5 ms^{-1}), which is due to the influence of ground returns on the Rayleigh response. The strong bias variations in the two range gates are related to the number and activity of the HPs in the respective Rayleigh ACCD rows. For instance, there were each three HPs in rows #3 and #5, including pixels [03,02], [03,14], and [05,10], which exhibited strong RTS fluctuations with average RTS level lifetimes of less than 20 h and step sizes of several tens of LSB (Table 3). The example depicted in Fig. 14 reveals the limitation of the DCMZ correction as well as the necessity to improve the data quality in reprocessing campaigns and the performance stability of the Aeolus-2 detector design.

7. ANOMALIES IN THE IMAGE ZONE

In addition to the analyses in lidar mode presented in the previous sections, the dark current properties were also sporadically assessed in imaging mode at times when the instrument was in LBWU mode, i.e., at the very beginning of the mission, during laser switch-overs, and in the frame of the EOL activities. In LBWU mode, the laser was not emitting UV pulses, and hence no atmospheric return signal was acquired. In imaging mode, 15 images were recorded per observation, which were individually read out without vertical integration of the signals and storage of the charges in the memory zone. Hence, in contrast to lidar mode, the signals on the 16 × 16 pixel of the image zone (Fig. 1) contained the information of the full atmospheric column without any range resolution, while the memory zone anomalies did not affect the signal levels.

Figure 15 depicts an example of an in-orbit dark current calibration (DCC) measurement performed on 31 August 2018, nine days after launch. It represents the raw dark signals on the ACCD image zone averaged over all 120 × 15 images (120 observations correspond to 24 min of measurements). Both detectors exhibited a vertical gradient of about $2e^-$ from top to bottom. The gradient was also present on the 2 × 2 virtual pixels at both edges of the ACCD (not shown), which represent the DCO, so that it was removed when applying DCO correction on the raw dark signals. The gradient was stable over the mission lifetime, although the DCO increased by about 2% on both detectors over the nearly five years. The DCO gradient most likely originated from variations in the bias voltage supply or clock waveforms over the course of the readout.

Apart from the vertical DCO gradient, a horizontal gradient from left to right was evident in the raw DCC signals, especially on the Mie channel. As the DCO correction was applied per row using the two post-scan pixels, the horizontal gradient was still present in the DCO-corrected signals. However, it was smaller ($<0.3e^-$ on both detectors) than the vertical gradient and also stable over the mission lifetime. The same holds true for the dark signal non-uniformity (DSNU) and the mean dark signal of the two detectors, which were $<0.2e^-$ in accordance with on-ground tests [54]. The horizontal gradient becomes more obvious in Fig. 16, which shows the dark current in the image zone of the Mie and Rayleigh ACCDs after subtraction of the DCO, obtained from DCC measurements on 31 August 2018 (top panels) and on 4 June 2023 (bottom panels). Note that the instrument was still in LBWU mode when the first DCC was carried out after launch, whereas it was in operation during the DCC in 2023. Therefore, a special timing setting had to be applied in a dedicated EOL test such that the imaging mode acquisition occurred before the atmospheric return reached the ACCD; hence this procedure was referred to as high-altitude DCC (Hi-DCC). DCCs below ground, in analogy to DUDEs, could not be executed due to limitations in the range of delay parameters of the detector acquisition. The Hi-DCC approach turned out to be a feasible calibration method and is thus recommended for Aeolus-2 to perform a regular DCC monitoring.

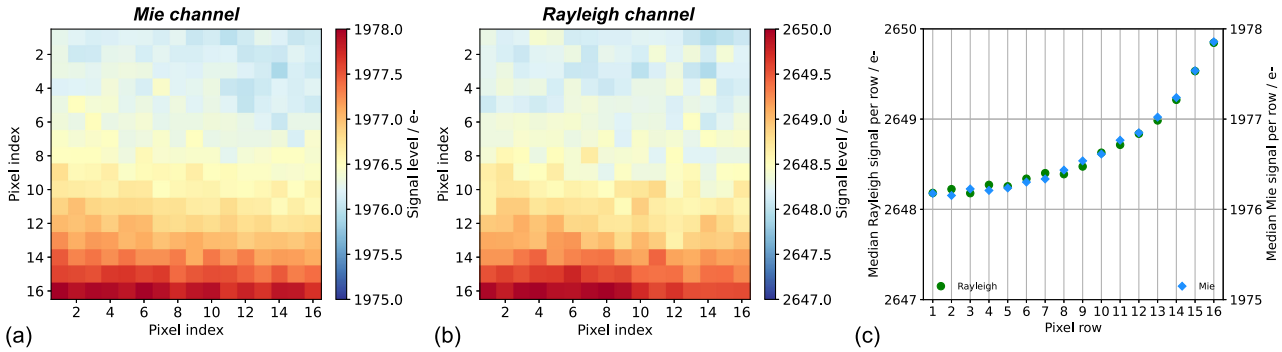

Fig. 15. Dark current calibration at the beginning of the mission on 31 August 2018, 9:15 UTC to 9:39 UTC: the raw signals including the detection chain offset on (a) Mie and (b) Rayleigh ACCD image zone exhibit a vertical gradient of about $2e^{-}$. The median signals per row are shown in panel (c).

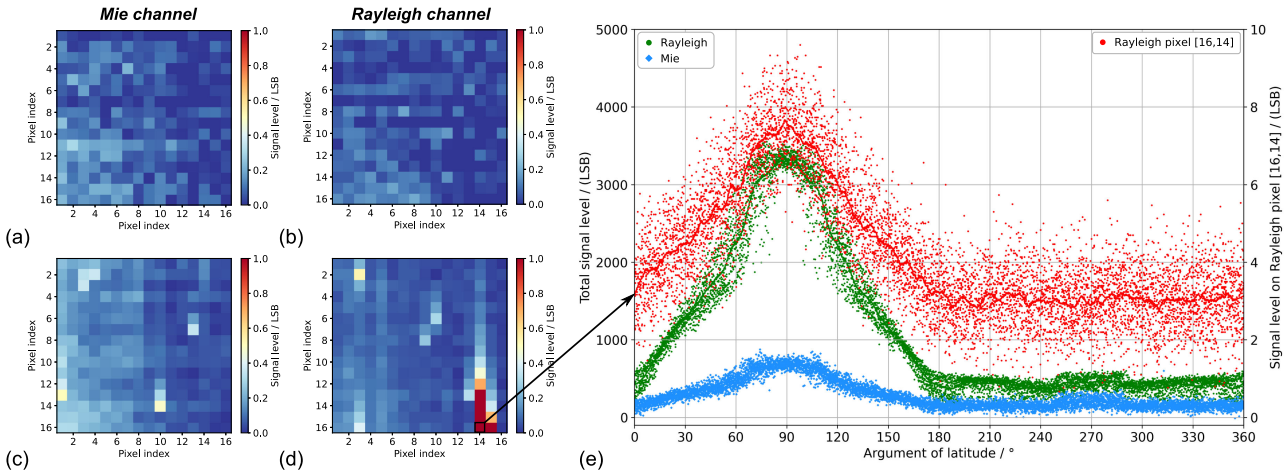

Fig. 16. Signal anomalies in the image zone: The left and middle panels depict the raw signal levels after DCO correction on (a), (c) Mie and (b), (d) Rayleigh ACCD measured in dark current calibration (DCC) mode at the beginning (31 August 2018) and the end of the mission (4 June 2023), respectively. The right panel (e) shows the orbital variation of the Rayleigh (green) and Mie signal levels (blue) together with those on Rayleigh pixel [16,14] (red), measured over multiple orbits in LBWU mode.

While the horizontal gradient in dark current was nearly constant over the mission lifetime, several pixel anomalies became visible on the DCC images measured during the EOL test on 4 June 2023 [Figs. 16(b) and 16(d)]. Most notably, enhanced signal levels appeared along certain columns of the image zone with decreasing intensity from the bottom to the top of the image (vertical smearing), which points to a charge transfer inefficiency (CTI) effect during the readout process when the charges were shifted to the memory transfer section row by row. The image zone anomaly was strongest in column #14 of the Rayleigh ACCD and was first observed in November 2018 in the images that were recorded in weekly activities performed in imaging mode aiming at the monitoring of the near-field laser beam profile and the optical alignment of the instrument. Starting from early May 2022, the neighboring column #15 was affected as well. The subsequent appearance of pixels with enhanced signal levels suggests radiation-induced detector defects to be the root cause, similar to the hot pixels in the memory zone. Further analysis showed that the signal intensity on the anomalous pixels was correlated with that on the right hemisphere of the Rayleigh image; i.e., it was fed by both solar background and atmospheric backscatter signals. This effect was verified by another EOL test, which was performed on 1 May 2023 when extended measurements were conducted in imaging mode over multiple orbits.

Figure 16(e) shows the orbital variation of the total signal levels that are measured on the image zone of the Rayleigh (green) and Mie ACCD (light blue) together with the signal levels that are detected on Rayleigh pixel [16,14] (red). The levels peaked around the North Pole at an argument of latitude of 90°, where the solar background was largest in May. In the Southern Hemisphere (180° to 360°), the measured signal was purely from atmospheric backscatter of the emitted laser pulses, accounting for ≈ 400 LSB on the Rayleigh channel and ≈ 200 LSB on the Mie channel, respectively, while the signal on the anomalous pixel was ≈ 3 LSB. Hence, the enhanced signal on Rayleigh pixel [16,14] was correlated with both the intensity of the solar background and the atmospheric backscatter. Further EOL tests at different frequency set points of the instrument finally showed that the signal intensities on the non-illuminated bottom pixels of column #14 of the Rayleigh ACCD scaled with those on the illuminated pixels of the same column at the location of the right Rayleigh spot associated with filter B (see Fig. 1). The results obtained from the different EOL activities

led to the conclusion that the image zone anomalies were very likely due to a non-perfect flushing process that left traces of the charges generated on the ACCD image zone during its illumination. The vertical smearing which suggests CTI in readout direction (row #16 is read out first, row #1 is read out last) supports this hypothesis of an inefficient flushing as a result of permanent damage, potentially caused by a cosmic ray event.

As the enhanced signal levels on the anomalous Rayleigh pixels in the image zone accounted for less than 1% of the total signal levels in the absence of solar background, the image zone anomalies were not seen in lidar mode after signal accumulation and are assumed to have had no significant impact on the quality of the Aeolus data products. However, they would have had a detrimental effect on the spectrometer response stability if the intensities had been higher. This is because a post-processing correction of the memory zone data would have been difficult without a regular monitoring of the imaging mode dark currents, since the two-dimensional information is lost during the accumulation process in the nominal wind measurement mode.

8. SUMMARY AND OUTLOOK

The Aeolus mission has successfully demonstrated that a Doppler wind lidar can be operated in space for several years, providing global wind profiles that significantly improve the accuracy of numerical weather forecasts. This achievement was accomplished despite the detector anomalies that were encountered during the nearly five-year mission lifetime, predominantly the 75 HPs on the memory zones of the two ACCDs, accounting for 10% of all pixels on the Mie and Rayleigh channel detectors. The essential measure to mitigate the associated large wind errors of several meters per second in certain altitude bins was the establishment of the DUDE calibration procedure to measure the dark current levels during laser operation, which was conducted more and more frequently over the course of the mission (up to eight times per day) at the expense of wind observations. In addition to the error reduction, the obtained DUDE dataset allowed for a classification of the HPs according to their dark current characteristics. The study revealed that most of the HPs (76%) exhibit RTS behavior, some of them showing complex temporal signatures with multiple RTS levels. Other HPs display slow drifts or rare shifts in the elevated dark current levels. A segmentation approach was applied to the dark current time series to derive statistical parameters, such as the most likely RTS step size and average lifetime of each HP. The analysis yielded step sizes ranging from a few to hundreds of electrons and typical lifetimes of tens of hours to a few days. These parameters are relevant for the Aeolus data quality, as they facilitate the distinction between real RTS transitions and atmospheric signal variations. This distinction is important in the data reprocessing to introduce additional DCMZ correction files between wind measurements at times when there was no DUDE procedure.

Following the end of the operational Aeolus mission in April 2023, a series of special in-orbit tests was carried out to address instrument-related and scientific investigations with regards to the Aeolus performance, data reprocessing, and preparation of future space lidar missions. In the frame of these activities, the temperature dependence of the dark current levels was investigated, revealing that the temperature coefficients of the hot pixels were systematically smaller by about 25% compared to the nominal pixels, hence supporting the assumption that the dark current anomalies were caused by radiation-induced displacement damages and not by CIC, which would be almost temperature-independent [55]. Moreover, the test allowed for the extrapolation to lower detector temperatures, predicting dark current rates of normal pixels as low as $0.017\,e^{-}s^{-1}$ at $-50°C$, which is the operating temperature envisaged for the follow-on mission Aeolus-2. Consequently, the dark current rates of two thirds of the HPs that had emerged during the Aeolus mission would be decreased to a level comparable to the dark current rates of normal pixels at $-30°C$. Nevertheless, the occurrence of RTS transitions and sporadic shifts in the dark current signals on different time scales would still remain an issue, albeit with a smaller impact on the wind results.

Further EOL tests have provided additional insights into the behavior of two special hot pixels on the Rayleigh ACCD whose activation was probably caused by a particularly strong exposure to cosmic radiation. As a result, these pixels were found to show smaller signal levels than expected from the signal levels on the pixels of the same ACCD columns. This charge storage anomaly introduced systematic wind errors that could not be tackled by the DCMZ correction. On the contrary, switching off the DCMZ correction for Rayleigh pixel [16,04] reduced the wind error in the corresponding range gate from about $7\ ms^{-1}$ to $1.5\ ms^{-1}$, as the signal loss on the pixel was partially compensated by retaining the elevated dark current.

The study of the charge storage ratio was then extended to all illuminated Rayleigh pixels, revealing a CSR non-uniformity of around $\pm 2\%$, which causes a range-gate-dependent bias of the Rayleigh wind results. Simulations of this phenomenon suggest bias variations of $\pm 2\ ms^{-1}$, which is larger than what was derived from observation minus background (O-B) statistics for a selected week in April 2023. Nevertheless, the impact of the CSR non-uniformity on the data quality will be the subject of further investigations during phase F of the Aeolus mission, which covers all activities after the end of the operational phase including data analysis and reprocessing, reporting, and archiving.

Another topic to be explored during phase F is the feasibility of applying a 1D fit to model the intensity distribution of the two Rayleigh spots while excluding hot pixels to derive the Rayleigh response from the intensity contrast between both spots. This approach is challenging due to the unknown actual fit function and the fact that non-Gaussian intensity distributions were observed during the Aeolus mission. These distributions were caused by temporally varying clipping of the atmospheric return signal and beam profile distortions. Hence, accurate modeling would require more fit parameters than there are illuminated pixels carrying the Rayleigh response information, given the coarse resolution of the ACCD image zone. For Aeolus-2, the planned ACCD image zone will have a similar number of columns, optimizing the compromise between resolution and readout noise—which scales with the number of pixels—and ensuring the atmospheric return signal is not distributed across too many pixels. By examining alternative fit functions, we aim to determine if the systematic errors from an imperfect fit are less significant than those stemming from

the current DCMZ correction. This investigation is particularly pertinent for the Rayleigh winds in range gate #16 following the signal charge storage anomaly on pixel [16,04] observed in December 2022. These efforts will guide the refinement of our methodologies and potentially improve the accuracy of Rayleigh wind measurements during Aeolus-2, where less clipping is expected, allowing for the assumption of a Gaussian signal distribution. Beyond developing suitable fit algorithms, an interesting and potentially beneficial approach involves implementing artificial intelligence and massive machine learning techniques. These methods can enhance accurate modeling, improve uncertainty handling, and enable scaling to larger datasets.

In addition to the memory zone anomalies, features in the ACCD image zone were presented in this work that can be regarded as a combination of detector and readout electronics anomalies. A vertical gradient of the DCO across the 16 rows of about 2 e^- is corrected by the DCO subtraction, which is applied row by row. This is not the case for the horizontal dark current gradient, which is less than 0.3 e^- over 16 pixels; however, its minuscule magnitude renders it negligible with regard to the data quality. The most striking image zone anomalies are enhanced signal levels along certain ACCD columns that appeared on more and more pixels over the course of the mission. The outcomes from several EOL activities suggest that the resulting vertical smearing patterns were very likely caused by an imperfect flushing during the readout process, leaving traces of the charges that were generated on the image zone during the illumination. Since the contribution to the total accumulated signal was less than 1%, it was not observed in lidar mode and also had no detrimental impact on the Aeolus data products.

The results of the present work are highly relevant for the forthcoming space lidar missions EarthCARE [56] and Aeolus-2, both working at the same UV wavelength and based on similar technology such as Aeolus [57,58]. For the latter, the Aeolus heritage will be largely retained, by employing ACCDs from Teledyne e2v with a very similar operating principle. As a consequence of the detrimental impact of the hot pixels on the Aeolus data quality, major efforts have been undertaken to resolve these issues in the preparation of Aeolus-2. Moreover, the need for higher vertical resolution of the wind profiles was expressed by both weather services and scientific users of the Aeolus data. Consequently, it was suggested to increase the number of atmospheric range gates from 24 to 66, while considering the reduction in signal-to-noise ratio in the shorter vertical samples. Most importantly, a buffer store will be added below the memory section that will enable readout between successive laser pulses. This not only reduces the noise on the wind channels, but also allows for intermediate DCMZ measurements without sacrificing observation time for the atmospheric signal, as was the case with the Aeolus operational correction scheme based on the DUDEs. In particular, it is intended to continuously monitor the dark current levels by means of a rolling DCMZ measurement where the dark current is recorded row by row during subsequent observations so that a complete DCMZ map for all 66 rows is obtained every 15 min [57].

As another improvement of the Aeolus-2 detectors, UV-optimized anti-reflection coatings are currently being explored in order to enhance the pixel quantum efficiency by 10% while improving the stability [58]. The thermal noise will be diminished by operating at lower temperature of −50°C, as demonstrated by the temperature extrapolation in Section 5. Finally, although CIC was ruled out as a root cause of the hot pixels thanks to the investigations of the temperature dependence, many of the potential architectures and design options that have been evaluated in the pre-development work of Aeolus-2 aimed at the reduction of CIC [58], which was considered a potential origin of the elevated dark signals apart from radiation-induced displacement defects.

Implementing an airborne demonstrator adapted to the Aeolus-2 design is currently discussed in the frame of risk reduction, as it would, like for Aeolus, provide comprehensive operational testing capabilities during mission preparation and execution, leveraging the full potential of the new design features including the advanced detectors and their new functional modes for performance monitoring and flexible signal acquisition strategies.

Aside from lidar space missions, the assessment of the Aeolus detector performance is also of relevance for other space instruments that are using CCD detectors. For instance, hot pixels in combination with RTS effects were observed on the CCD detectors of the Global Ozone Monitoring by Occultation of Stars (GOMOS) instrument on board ENVISAT deteriorating the ozone retrieval [59]. Analysis of the temperature dependence of the dark current in BRIght Target Explorer (BRITE) nanosatellite image sensors yielded activation energies of around 0.7 eV, similar to what was derived for the Aeolus HPs. This value points to the generation of PV pairs in both detectors that are common in proton-irradiated CCD matrices [60]. Finally, HPs were identified in CCDs of star trackers, e.g., those installed in the Solar Dynamics Observatory (SDO), necessitating a special algorithm to distinguish them from star images and to exclude them from the star tracker processing [61]. The examples provided above, along with the findings of this study, underscore the ongoing necessity to investigate anomalies in CCDs operated in space and to develop strategies for their mitigation.

Funding. European Space Agency (40000126336/18/I-BG, 4000144330/24/I-AG).

Acknowledgment. The authors are grateful to Michael Rennie from the European Centre for Medium-Range Weather Forecasts (ECMWF) for the helpful discussions about the impact of the hot pixels on the Aeolus wind data quality. The authors also thank all partners involved in the planning, execution, and analysis of the Aeolus end-of-life activities: the Aeolus Flight Operation Segment (FOS), the Aeolus Mission Management and Planning Facility (MMPF), the Aeolus Payload Data Ground Segment (PDGS), Leonardo S.p.A., Airbus Italia, Airbus Defence and Space (Toulouse), Airbus Defence and Space (Stevenage), the European Space Research and Technology Centre (ESTEC), and the Data Innovation and Science Cluster (DISC). Their teamwork and dedication were instrumental in the successful completion of the tests.

Disclosures. The authors declare no conflicts of interest.

Data availability. The presented work includes data of the Aeolus mission, which is part of the European Space Agency (ESA) Earth Explorer Programme. This includes the L2B wind product (Baselines 15 and 16) that is publicly available and can be accessed via the ESA Aeolus Online Dissemination System ([62]). The processor development, improvement, and product reprocessing preparation have been performed by the Aeolus DISC, which involves DLR, DoRIT, TROPOS, ECMWF, KNMI, CNRS, S&T, ABB, and Serco, in close cooperation with the Aeolus PDGS.

REFERENCES

1. E. Andersson and P. Clissold, eds., "ADM-Aeolus science report," ESA SP-1311 (ESA Communications Production Office, 2008).
2. O. Reitebuch, "The spaceborne wind lidar mission ADM-Aeolus," in *Atmospheric Physics: Background–Methods–Trends*, U. Schumann, ed. (Springer, 2012), pp. 815–827.
3. O. Lux, D. Wernham, P. Bravetti, *et al.*, "High-power and frequency-stable ultraviolet laser performance in space for the wind lidar on Aeolus," Opt. Lett. **45**, 1443–1446 (2020).
4. A. Stoffelen, J. Pailleux, E. Källén, *et al.*, "The atmospheric dynamics mission for global wind field measurement," Bull. Am. Meteorol. Soc. **86**(1), 73–88 (2005).
5. O. Lux, C. Lemmerz, F. Weiler, *et al.*, "Retrieval improvements for the ALADIN Airborne Demonstrator in support of the Aeolus wind product validation," Atmos. Meas. Tech. **15**, 1303–1331 (2022).
6. F. Ehlers, T. Flament, A. Dabas, *et al.*, "Optimization of Aeolus' aerosol optical properties by maximum-likelihood estimation," Atmos. Meas. Tech. **15**, 185–203 (2022).
7. F. Weiler, M. Rennie, T. Kanitz, *et al.*, "Correction of wind bias for the lidar on board Aeolus using telescope temperatures," Atmos. Meas. Tech. **14**, 7167–7185 (2021).
8. O. Lux, C. Lemmerz, F. Weiler, *et al.*, "ALADIN laser frequency stability and its impact on the Aeolus wind error," Atmos. Meas. Tech. **14**, 6305–6333 (2021).
9. A. Martin, M. Weissmann, and A. Cress, "Investigation of links between dynamical scenarios and particularly high impact of Aeolus on numerical weather prediction (NWP) forecasts," Weather Clim. Dyn. **4**, 249–264 (2023).
10. V. Pourret, M. Šavli, J.-F. Mahfouf, *et al.*, "Operational assimilation of Aeolus winds in the Météo-France global NWP model ARPEGE," Q. J. R. Meteorol. Soc. **148**, 2652–2671 (2022).
11. M. P. Rennie, L. Isaksen, F. Weiler, *et al.*, "The impact of Aeolus wind retrievals on ECMWF global weather forecasts," Q. J. R. Meteorol. Soc. **147**, 3555–3586 (2021).
12. M. Rennie and L. Isaksen, *The NWP impact of Aeolus Level-2B winds at ECMWF* (2024).
13. C.-C. Chou, P. J. Kushner, S. Laroche, *et al.*, "Validation of the Aeolus Level-2B wind product over Northern Canada and the Arctic," Atmos. Meas. Tech. **15**, 4443–4461 (2022).
14. B. Witschas, C. Lemmerz, A. Geiß, *et al.*, "Validation of the Aeolus L2B wind product with airborne wind lidar measurements in the polar North Atlantic region and in the tropics," Atmos. Meas. Tech. **15**, 7049–7070 (2022).
15. M. Ratynski, S. Khaykin, A. Hauchecorne, *et al.*, "Validation of Aeolus wind profiles using ground-based lidar and radiosonde observations at Réunion island and the Observatoire de Haute-Provence," Atmos. Meas. Tech. **16**, 997–1016 (2023).
16. J. Abril-Gago, P. Ortiz-Amezcua, D. Bermejo-Pantaleón, *et al.*, "Validation activities of Aeolus wind products on the southeastern Iberian Peninsula," Atmos. Chem. Phys. **23**, 8453–8471 (2023).
17. H. Baars, J. Walchester, E. Basharova, *et al.*, "Long-term validation of Aeolus L2B wind products at Punta Arenas, Chile, and Leipzig, Germany," Atmos. Meas. Tech. **16**, 3809–3834 (2023).
18. S. Kirkwood, E. Belova, P. Voelger, *et al.*, "Extended validation of Aeolus winds with wind-profiling radars in Antarctica and Arctic Sweden," Atmos. Meas. Tech. **16**, 4215–4227 (2023).
19. M. Borne, P. Knippertz, M. Weissmann, *et al.*, "Validation of Aeolus L2B products over the tropical Atlantic using radiosondes," Atmos. Meas. Tech. **17**, 561–581 (2024).
20. P. Flamant, J. Cuesta, M.-L. Denneulin, *et al.*, "ADM-Aeolus retrieval algorithms for aerosol and cloud products," Tellus A **60**, 273–286 (2008).
21. A. Ansmann, U. Wandinger, O. Le Rille, *et al.*, "Particle backscatter and extinction profiling with the spaceborne high-spectral-resolution Doppler lidar ALADIN: methodology and simulations," Appl. Opt. **46**, 6606–6622 (2007).
22. C. J. Wright, R. J. Hall, T. P. Banyard, *et al.*, "Dynamical and surface impacts of the January 2021 sudden stratospheric warming in novel Aeolus wind observations, MLS and ERA5," Weather Clim. Dyn. **2**, 1283–1301 (2021).
23. M. Ern, M. A. Diallo, D. Khordakova, *et al.*, "The quasi-biennial oscillation (QBO) and global-scale tropical waves in Aeolus wind observations, radiosonde data, and reanalyses," Atmos. Chem. Phys. **23**, 9549–9583 (2023).
24. T. P. Banyard, C. J. Wright, S. M. Osprey, *et al.*, "Aeolus wind lidar observations of the 2019/2020 quasi-biennial oscillation disruption with comparison to radiosondes and reanalysis," Atmos. Chem. Phys. **24**, 2465–2490 (2024).
25. S. Khaykin, B. Legras, S. Bucci, *et al.*, "The 2019/20 Australian wildfires generated a persistent smoke-charged vortex rising up to 35 km altitude," Commun. Earth Environ. **1**, 22 (2020).
26. G. Dai, K. Sun, X. Wang, *et al.*, "Dust transport and advection measurement with spaceborne lidars ALADIN and CALIOP and model reanalysis data," Atmos. Chem. Phys. **22**, 7975–7993 (2022).
27. R. Song, A. Povey, and R. G. Grainger, "Characterisation of dust aerosols from ALADIN and CALIOP measurements," EGUsphere **17**, 2521–2538 (2023).
28. K. Sun, G. Dai, S. Wu, *et al.*, "Effect of wind speed on marine aerosol optical properties over remote oceans with use of spaceborne lidar observations," Atmos. Chem. Phys. **24**, 4389–4409 (2024).
29. O. Reitebuch, C. Lemmerz, O. Lux, *et al.*, "Initial assessment of the performance of the first wind lidar in space on Aeolus," in *EPJ Web of Conferences* (EDP Sciences, 2020), Vol. **237**, p. 01010.
30. F. Weiler, T. Kanitz, D. Wernham, *et al.*, "Characterization of dark current signal measurements of the ACCDs used on board the Aeolus satellite," Atmos. Meas. Tech. **14**, 5153–5177 (2021).
31. G. Hopkinson, C. Dale, and P. Marshall, "Proton effects in charge-coupled devices," IEEE Trans. Nucl. Sci. **43**, 614–627 (1996).
32. P. Anderson, F. Rich, and S. Borisov, "Mapping the South Atlantic Anomaly continuously over 27 years," J. Atmos. Sol. Terr. Phys. **177**, 237–246 (2018).
33. K. A. Nasuddin, M. Abdullah, and N. S. Abdul Hamid, "Characterization of the South Atlantic Anomaly," Nonlinear Processes Geophys. **26**, 25–35 (2019).
34. R. A. Kimble, P. Goudfrooij, and R. L. Gilliland, "Radiation damage effects on the CCD detector of the space telescope imaging spectrograph," Proc. SPIE **4013**, 532–544 (2000).
35. V. Noel, H. Chepfer, C. Hoareau, *et al.*, "Effects of solar activity on noise in CALIOP profiles above the South Atlantic Anomaly," Atmos. Meas. Tech. **7**, 1597–1603 (2014).
36. B. Liu, Y. Li, L. Wen, *et al.*, "Effects of hot pixels on pixel performance on backside illuminated complementary metal oxide semiconductor (CMOS) image sensors," Sensors **23**, 6159 (2023).
37. J. A. McKay, "Modeling of direct detection Doppler wind lidar. II. The fringe imaging technique," Appl. Opt. **37**, 6487–6493 (1998).
38. M. L. Chanin, A. Garnier, A. Hauchecorne, *et al.*, "A Doppler lidar for measuring winds in the middle atmosphere," Geophys. Res. Lett. **16**, 1273–1276 (1989).
39. C. Flesia and C. L. Korb, "Theory of the double-edge molecular technique for Doppler lidar wind measurement," Appl. Opt. **38**, 432–440 (1999).
40. U. Marksteiner, "Airborne wind lidar observations for the validation of the ADM-Aeolus instrument," Dissertation (Technische Universität München, 2013).
41. J. R. Janesick, ed., *Scientific Charge-coupled Devices* (SPIE, 2001).
42. C. Truong, L. Oudre, and N. Vayatis, "Selective review of offline change point detection methods," Signal Process. **167**, 107299 (2020).
43. F. Weiler, "Detecting hot pixel induced steps in the Aeolus atmospheric signals," Master thesis (University of Innsbruck, 2021).
44. O. Reitebuch, C. Lemmerz, E. Nagel, *et al.*, "The airborne demonstrator for the direct-detection Doppler wind lidar ALADIN on ADM-Aeolus. Part I: instrument design and comparison to satellite instrument," J. Atmos. Ocean. Technol. **26**, 2501–2515 (2009).
45. O. Lux, C. Lemmerz, F. Weiler, *et al.*, "Airborne wind lidar observations over the North Atlantic in 2016 for the pre-launch validation of the satellite mission Aeolus," Atmos. Meas. Tech. **11**, 3297–3322 (2018).
46. O. Lux, C. Lemmerz, F. Weiler, *et al.*, "Intercomparison of wind observations from the European Space Agency's Aeolus satellite mission and the ALADIN Airborne Demonstrator," Atmos. Meas. Tech. **13**, 2075–2097 (2020).

47. R. Widenhorn, M. M. Blouke, A. Weber, *et al.*, "Temperature dependence of dark current in a CCD," Proc. SPIE **4669**, 193–201 (2002).
48. A. D. Holland, "Annealing of proton-induced displacement damage in CCDs for space use," in *Photoelectric Image Devices, the McGee Symposium*, B. L. Morgan, ed. (1991).
49. G. R. Hopkinson, "Space radiation effects on CCDs," in *ESA Special Publication*, B. Kaldeich-Schürmann, ed., Vol. **313** of ESA Special Publication (1991), pp. 301–306.
50. G. Hopkinson and A. Mohammadzadeh, "Comparison of CCD damage due to 10- and 60-MeV protons," IEEE Trans. Nucl. Sci. **50**, 1960–1967 (2003).
51. F. Weiler, N. Masoumzadeh, and O. Reitebuch, "Correction of hot pixel steps in Aeolus reprocessed data," *Aeolus 3rd Anniversary Conference*, Taormina, Italy, 28 March–1 April 2022.
52. G.-J. Marseille, J. de Kloe, A. Dabas, *et al.*, "Aeolus Rayleigh-channel winds in cloudy conditions," Q. J. R. Meteorol. Soc. **149**, 3270–3289 (2023).
53. T. Flament, D. Trapon, A. Lacour, *et al.*, "Aeolus L2A aerosol optical properties product: standard correct algorithm and Mie correct algorithm," Atmos. Meas. Tech. **14**, 7851–7871 (2021).
54. N. Masoumzadeh, F. Weiler, I. Krisch, *et al.*, "Noise characterization of the ACCDs detectors onboard ESA's Wind Lidar Mission Aeolus," *Aeolus 3rd Anniversary Conference*, Taormina, Italy, 28 March–1 April 2022.
55. N. Bush, J. Heymes, D. Hall, *et al.*, "Measurement and optimization of clock-induced charge in electron multiplying charge-coupled devices," J. Astron. Telesc. Instrum. Syst. **7**, 016002 (2021).
56. A. J. Illingworth, H. W. Barker, A. Beljaars, *et al.*, "The EarthCARE satellite: the next step forward in global measurements of clouds, aerosols, precipitation, and radiation," Bull. Am. Meteorol. Soc. **96**(8), 1311–1332 (2015).
57. D. Wernham, A. Heliere, G. Mason, *et al.*, "Status of Aeolus-2 pre-development activities," *Aeolus 3rd Anniversary Conference*, Taormina, Italy, 28 March–1 April 2022.
58. A. Heliere, D. Wernham, G. Mason, *et al.*, "Status of Aeolus-2 mission pre-development activities," Proc. SPIE **12777**, 1277709 (2023).
59. P. Keckhut, A. Hauchecorne, L. Blanot, *et al.*, "Mid-latitude ozone monitoring with the GOMOS-ENVISAT experiment version 5: the noise issue," Atmos. Chem. Phys. **10**, 11839–11849 (2010).
60. A. Popowicz, "Analysis of dark current in BRITE nanostellite CCD sensors," Sensors **18**, 479 (2018).
61. D. Felikson, M. Ekinci, J. Hashmall, *et al.*, "On-orbit solar dynamics observatory (SDO) star tracker warm pixel analysis," *AIAA Guidance, Navigation, and Control Conference*, Portland, Oregon, 8–11 August 2011.
62. https://aeolus-ds.eo.esa.int/oads/access/collection/L1B_L2_Products